#### Observing GAMA-23 field with uGMRT Band-2

M.Sc. Thesis

By: Gitaj Singh



# DEPARTMENT OF ASTRONOMY , ASTROPHYSICS AND SPACE ENGINEERING

# INDIAN INSTITUTE OF TECHNOLOGY INDORE

May, 2025

#### Observing GAMA-23 field with uGMRT Band-2

#### **A THESIS**

Submitted in fulfillment of the requirements for the award of the degree

of

**Master of Science in Astronomy** 

by

Gitaj Singh



# DEPARTMENT OF ASTRONOMY , ASTROPHYSICS AND SPACE ENGINEERING

# INDIAN INSTITUTE OF TECHNOLOGY INDORE

May, 2025



#### INDIAN INSTITUTE OF TECHNOLOGY INDORE

#### CANDIDATE'S DECLARATION

I hereby certify that the work which is being presented in the thesis entitled **Observing GAMA-23** field using uGMRT band-2 in the partial fulfillment of the requirements for the award of the degree of MASTER OF SCIENCE and submitted in the DEPARTMENT OF ASTRONOMY, ASTROPHYSICS AND SPACE ENGINEERING, Indian Institute of Technology Indore, is an authentic record of my own work carried out during the time period from July, 2023 to May, 2025 under the supervision of Dr. Abhirup Datta, Dean, Research and Development, Indian Institute of Technology Indore.

The matter presented in this thesis has not been submitted by me for the award of any other degree of this or any other institute.

(gitaj fingh.

Signature of the student with date

Gitaj Singh

This is to certify that the above statement made by the candidate is correct to the best of my/our knowledge.

> 19/05/2025 Signature of the Supervisor of

M.Sc. thesis

Dr. Abhirup Datta

Gitaj Singh has successfully given his/her M.Sc. Oral Examination held on 05/05/2025.

Signature(s) of Supervisor(s) of MSc thesis

Date: 19/05/2025

Manauerta Chakraborty Convenor, DPGC

Date: 19/05/2025

Program Coordinator, M.Sc.

Manoueta Chakraborty

Date: 19/05/2025

( Doy

HoD, DAASE

Date:19/05/2025

#### **ACKNOWLEDGEMENT**

First and foremost, I would like to express my deepest gratitude to my supervisor, Dr. Abhirup Datta, for his exceptional guidance, encouragement, and support throughout the course of my research. His insightful feedback, patient mentoring, and constant motivation have played a pivotal role in shaping both the direction and the quality of this thesis. Working under his supervision has been an enriching experience that has greatly contributed to my academic and personal growth.

I am sincerely thankful to Ms. Rashmi Sagar for her mentorship and invaluable advice. Her clarity of thought, supportive nature, and willingness to share knowledge have had a significant impact on my learning. Her guidance has helped me develop a more thoughtful and structured approach towards research.

I would also like to thank my friends Vishruth, Vijay, Prasad, Parth, Hari, Amar, Devesh, Aryan, Annie, Anushka, Ashutosh, Daisy, and Navanit for their camaraderie and friendship. Their support—whether during long hours at the lab, late-night discussions, or moments of doubt—made this journey not only bearable but memorable.

In addition, I am grateful to all the faculty members of the Department of Astronomy, Astrophysics, and Space Engineering at IIT Indore. Their teaching, guidance, and constructive feedback over the years have helped me broaden my understanding of the field and inspired me to pursue research with curiosity and commitment.

Finally, I would like to thank everyone who has been a part of this journey in one way or another. Your support has meant a great deal to me.

#### **ABSTRACT**

The GAMA-23 field is a promising region for studying the Epoch of Reionization (EoR), a key phase in the evolution of the Universe when the first luminous sources ionized the intergalactic medium (IGM). Thanks to its extensive multi-wavelength coverage and accessibility to low-frequency radio observations, GAMA-23 allows for detailed investigations of the 21 cm signal, which traces neutral hydrogen in the early Universe. In this thesis, we used data from the upgraded Giant Metrewave Radio Telescope (uGMRT) in Band-2 (120–250 MHz) to detect faint radio signals and improve our understanding of ionization and galaxy formation during cosmic history.

Due to heavy radio frequency interference (RFI) caused by the low elevation of the source from the GMRT site, the legacy GMRT software backend (GSB) data was unusable. Instead, we used data from the GMRT Wideband Backend (GWB), which we split into sub-bands and processed using the SPAM pipeline. SPAM includes both direction-independent and direction-dependent calibration, and it corrects for ionospheric phase errors using the peeling technique. A TGSS-based sky model was used as a reference during the calibration. After calibrating the individual sub-bands, we used WSClean for wideband imaging, which resulted in a high-resolution image with an off-source RMS noise of 316 μJy/beam and a resolution of 15.35"× 8.22".

We then performed source detection and created a source catalog, which was cross-matched with several existing radio surveys (TGSS, NVSS, SUMSS, RACS, and GLEAM) to check for positional accuracy and flux consistency. The comparison showed good agreement with previous surveys, indicating that our calibration and imaging were successful. We also calculated differential source counts at 183 MHz, correcting for false detections and incompleteness using simulations. The source counts match well with predictions from models like *S*<sup>3</sup>-SKADS and T-RECS, as well as previous observational results. Overall, the results of this work add to our understanding of faint radio sources, star formation, and the evolution of galaxies in the early Universe.

## **Contents**

Lis	st of I	Figures		VI
Lis	st of T	<b>Fables</b>		VIII
1	Intr	oductio	n	1
	1.1	Radio	Astronomy	. 1
		1.1.1	Radio Telescopes	. 3
		1.1.2	Interferometry	. 4
	1.2	The G	iant Meter Radio Telescope (GMRT)	. 5
	1.3	Radio	Surveys	. 7
	1.4	TIFR (	GMRT Sky Survey (TGSS)	. 8
2	Gala	axy and	Mass Assembly (GAMA) Fields	11
	2.1	GAMA	A 23 Field	. 11
	2.2	Multi-	Wavelength Studies of GAMA-23	. 13
3	Rad	io Inter	ferometric Data Analysis	17
	3.1	Measu	rements from a Radio Interferometer	. 17
		3.1.1	Coordinate systems	. 18
		3.1.2	Delayed correction	. 19
3.2 Imaging			ng	. 20
	3.3	Calibra	ation	. 22
		3.3.1	Gain Solution	. 22
		3.3.2	Standard Calibration	. 23
		3.3.3	Self Calibration	. 24
		3.3.4	Direction Dependent Calibration	. 24
	3 4	Data re	eduction using SPAM	26

	3.5	uGMRT Observation	8
4	Disc	ussions and Results 2	9
	4.1	Data analysis	9
	4.2	Comparison with other Radio Catalogs	2
		4.2.1 Flux Density Offset	2
		4.2.2 Positional Accuracy	5
		4.2.3 Spectral Index Distribution	6
	4.3	Source Count	6
		4.3.1 False Detection Rate	7
		4.3.2 Completeness Correction	8
		4.3.3 Differential Source Count	9
5	Con	dusion 4	2
	5.1	Summary of Results	.2
	5.2	Scientific Implications	.3
	5.3	Future Prospects	4
	5.4	Concluding Remarks	-5
Bi	bliogi	aphy 4	6

# **List of Figures**

1.1	A basic dish radio telescope. The parabolic dish collects
	radio waves and reflects them to a focal point, where a re-
	ceiver detects and amplifies the signal for further analysis.
	Credit: Britannica encyclopedia
1.2	GMRT array consisting of 30 antennas and their locations.
	From Gupta et al.(9)
1.3	Wide bandwidth of GMRT before and after the upgrade.
	This image is taken from Buch et al.(10) 6
1.4	Comparison of current and planned radio interferometers'
	continuum sensitivities for a 9-hour on-source integration.
	The GMRT, VLA, JVLA, uGMRT, LOFAR, MeerKAT, ASKAP,
	and SKA-1-Mid sensitivities are displayed by the points. As
	may be observed, until Phase-1 of the SKA is implemented,
	uGMRT is the world's most sensitive interferometer at fre-
	quencies between 250 and 1500 MHz (9)
1.5	RMS noise level map for TGSS in ADR (22)
2.1	An image of GAMA 23 field centered at $\alpha_{J2000} = 23h00m00s$
	and $\delta_{J2000} = -32^{\circ}30'00''$ . This image was obtained from
	the TGSS Alternative Data Release (22). The off-source
	RMS noise value is 3.5 mJy/beam
2.2	"Stellar mass in units of $log(M/M_{\odot})$ vs redshift for the 936
	MHz/G23 sources (red), and for all G23 galaxies (grey).
	This shows that galaxies with detected radio emission are
	mainly galaxies with larger masses" (13)
3.1	Steps taken during self-calibration. Credit: NRAO 25

4.1	UV coverage of the dataset before applying calibration	. 30
4.2	The final wideband image of the GAMA 23 field. The Flux	
	density is in the unit of Jansky per beam. The off-source	
	RMS noise value is 316 µJy/beam, and the resolution is	
	15.35"×8.22"	. 31
4.3	The compared flux densities of the GAMA-23 band image	
	at 183 MHz with other catalogs	. 34
4.4	Comparison of predicted and observed flux densities at 183	
	MHz. The predicted fluxes are derived using a spectral in-	
	dex 0.73 estimated from RACS and NVSS catalogues	. 34
4.5	Offset of the source RA and Dec for the 183 MHz catalog	
	from different catalogs	. 35
4.6	Normalized distribution of spectral index measurements in	
	the field, obtained by cross-matching with RACS using a 5"	
	matching radius. The black dashed line indicates a spectral	
	index of -0.7	. 37
4.7	Euclidean normalised differential source counts at 183 MHz	
	for the GAMA-23 field from this work (red circles), cor-	
	rected for false detections and incompleteness. These are	
	compared with simulated models — $S^3$ (Wilman et al. 2008;	
	black dashed line) and T-RECS (Bonaldi et al. 2019; yellow	
	dashed line). Also shown for comparison are previous ob-	
	servational results: ELAIS-N1 (Chakraborty et al. 2019;	
	olive green diamonds), Lockman Hole (Mazumder et al.	
	2020), ELAIS-N1 (Ocran et al. 2020), ELAIS-N1 (Sabater	
	et al. 2021), GAMA-23 (Gürkan et al. 2022), and BOOTES	
	(Sinha et al. 2023)	11

## **List of Tables**

2.1	GAMA survey regions with RA and Dec ranges and main	
	survey limits	12
2.2	Summary of properties of the radio surveys covering GAMA-	
	23 (14)	15
3.1	Observation summary for GWB data	28
4.1	Comparison of radio surveys with their telescope, frequency,	
	resolution, and noise levels	32
4.2	Median astrometric offsets of the uGMRT 183 catalogue	
	relative to RACS and NVSS, along with their respective	
	central frequencies.	36

## **Chapter 1**

#### Introduction

#### 1.1 Radio Astronomy

Radio astronomy began when Karl Jansky, who was employed by the Bell Telephone Laboratories, conducted his experiment. He conducted the experiment to find a way to detect far-off thunderstorm static, which interfered with telephone connections. During the experiment, Jansky identified three types of static: one from local thunderstorms, another from tropical thunderstorms, and a third from a completely unknown source. The latter source changed its position over a 24-hour period, moving through all compass directions. After ruling out the Sun as the cause, Jansky concluded that the source of the radiation was located beyond our solar system. He identified it as being at the center of the Milky Way galaxy and speculated that the radiation might be coming from interstellar material.

Every celestial body emits electromagnetic waves; however, Earth's atmosphere is opaque to wavelengths shorter than ultraviolet, and shorter wavelengths are much more susceptible to atmospheric attenuation, which leaves radio waves an excellent candidate for terrestrial-based astronomy.

Radio waves can penetrate dense gas clouds that block visible light and other shorter wavelengths. These clouds often obscure regions of space where stars are forming or where galaxies and other celestial structures are hidden. Since radio waves can travel through such obstacles with minimal attenuation, they allow astronomers to study the interiors of star-forming regions, observe the structure of distant galaxies, and even map the cosmic

microwave background.

There are two types of radio radiation:

- Continuum Radiation: These emissions cover a broad range of wavelengths and can be detected at any wavelength. They can be either thermal (e.g., blackbody radiation) or non-thermal (e.g., bremsstrahlung, synchrotron radiation)
- Line Radiation: These originate from transitions within atoms and molecules and can only be detected using a narrow band about a particular frequency. They can be detected both in absorption and emission, e.g., in the H21 cm line.

The following are some of the physical origins of radio radiation observed in astronomical sources:

- Thermal Radiation (Blackbody Radiation): These are the emissions caused by the thermal energy of a body. e.g., stars, nebulae, or accretion disks.
- Non-Thermal Radiation (Bremsstrahlung): These emissions are caused by the deceleration of high-energy electrons
- **Synchrotron Radiation**: These emissions are caused by the acceleration of relativistic electrons under the influence of a magnetic field. These are typically observed in pulsars, active galactic nuclei (AGN), and radio galaxies.
- **Compton Scattering**: These are caused by the scattering of highenergy electrons and low-energy photons, which increases the energy and, thereby, frequency of the photons.
- **Spectral-Line Absorption**: Absorption lines seen against a background of continuum emission (e.g., HI region)
- **Spectral-Line Emission**: Line emissions produced from the transition in atoms or molecules.

#### 1.1.1 Radio Telescopes

Radio telescopes are used to collect the incoming radio waves and convert them into an electrical signal, which can be used for further analysis. They consist of an antenna that collects the radio signal and a receiver for processing the signal.

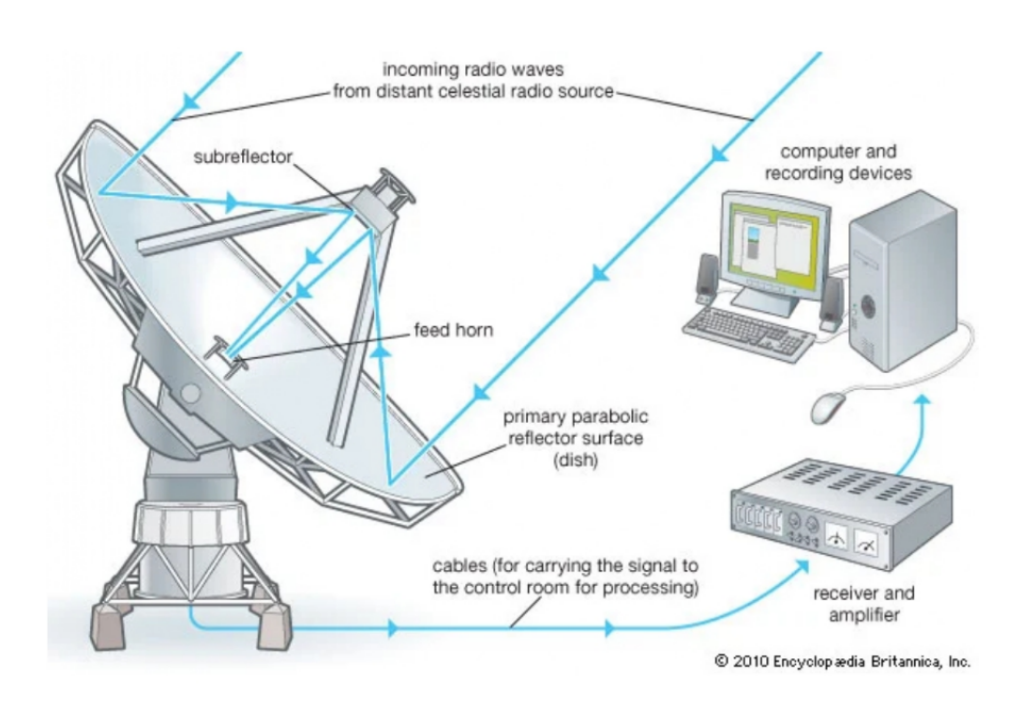


**Figure 1.1:** A basic dish radio telescope. The parabolic dish collects radio waves and reflects them to a focal point, where a receiver detects and amplifies the signal for further analysis. Credit: Britannica encyclopedia

The basic components of a radio telescope are explained below:

- Antenna: The antenna takes the radio waves and converts them into electrical signals. An antenna in its basic form is just a conductor being bombarded with electromagnetic waves; the electromagnetic field in the electromagnetic waves causes the electrons in the conductor to move, producing an electrical current. There are many kinds of antennas used, such as parabolic, monopole, dipole, horn antenna, etc.
- Data Processing: The incoming weak electrical signal is amplified using a Low Noise Amplifier, and then the signal is passed through a mixer, which lowers the frequency of the signal so that it can be processed further.

#### 1.1.2 Interferometry

The resolving power of a single dish is given by:

$$hetapproxrac{\lambda}{D}$$

Where:

- $\theta$  is the angular resolution (in radians),
- $\lambda$  is the observed wavelength,
- *D* is the diameter of the dish.

At 21 cm, the size of the dish required for a resolution of 1 arc minute, a dish of 721 m in diameter is required, which is physically impractical. Therefore, a number of antennas are combined in an array to synthesize a telescope with a larger aperture; this is known as aperture synthesis. Due to the different points of view of different antennas and their different positions compared to the source, each signal is phase-shifted. When the signals from a pair of antennas are combined, a fringe pattern is obtained due to interference. This fringe pattern is equivalent to a Fourier component of the source. By combining more of these fringe patterns, we can get the image

of the source. As the earth rotates, the position of the antennas changes with respect to the source, thereby giving more fringe patterns, increasing our coverage of the Fourier plane, and increasing the image quality; this is known as rotation synthesis.

For an interferometer array, the resolving power depends on the maximum baseline length *B* between antennas:

$$hetapproxrac{\lambda}{R}$$

Here, *B* can be much larger than the diameter of any individual dish, enabling far greater resolution than a single-dish telescope.

#### **1.2** The Giant Meter Radio Telescope (GMRT)

The Giant Meter Radio Telescope (GMRT) is one of the world's largest and most sensitive operational low-frequency radio telescopes. It comprises 30 antennas spread out over a 25-kilometer radius, each with a 45-meter diameter. At meter wavelengths, this arrangement provides a total collecting area of around 30,000 square meters and attains an angular precision of about one arc second. The central region comprises 12 of the 30 dishes in a  $1\times1$  sq. km area, and the rest are scattered in 'Y' shaped arms, as can be seen in Figure 1.2. Legacy GMRT could be observed in a frequency band of 130-170 MHz, 225-245 MHz, 300-360 MHz, 580-660 MHz, and 1000-1450 MHz.

GMRT has been upgraded to improve the antenna's sensitivity by a factor of up to three and to keep it relevant in the SKA era. The upgraded GMRT achieves seamless frequency coverage and broad bandwidths by implementing feeds and front-end electronics designed to operate across octave frequency ranges. This has enabled it to be "the most sensitive interferometer in the world at frequencies 250-1500 MHz" (9), as can be seen in Figure 1.4. This capability is further enhanced by a wide-band optical fiber transmission system, which efficiently transfers radio frequency (RF) signals from the antennas to the central receiver building. At the central location, advanced wide-band analog and digital back-ends support this functionality. The finalized frequency bands for the uGMRT are 50–80 MHz

(Band 1), 120–250 MHz (Band 2), 250–500 MHz (Band 3), 550–850 MHz (Band 4), and 1050–1450 MHz (Band 5) (9).

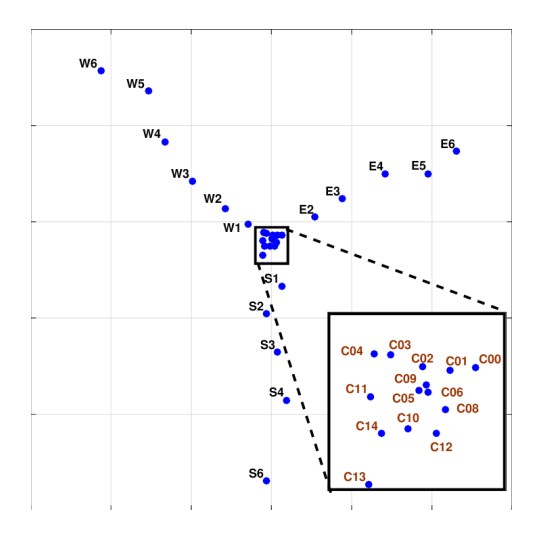


**Figure 1.2:** GMRT array consisting of 30 antennas and their locations. From Gupta et al.(9).

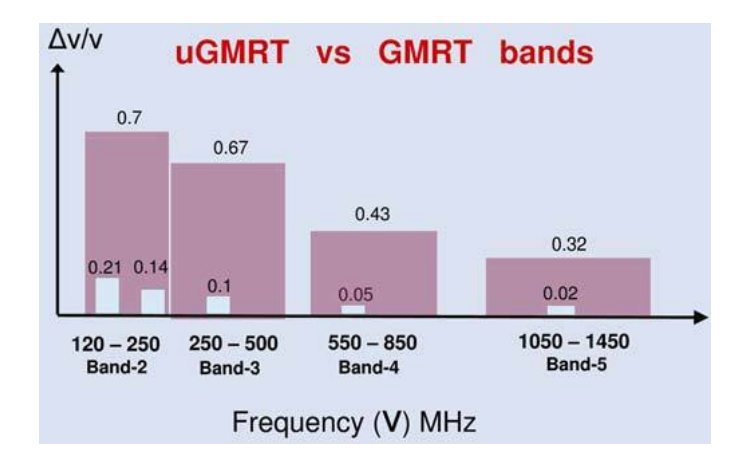


**Figure 1.3:** Wide bandwidth of GMRT before and after the upgrade. This image is taken from Buch et al.(10).

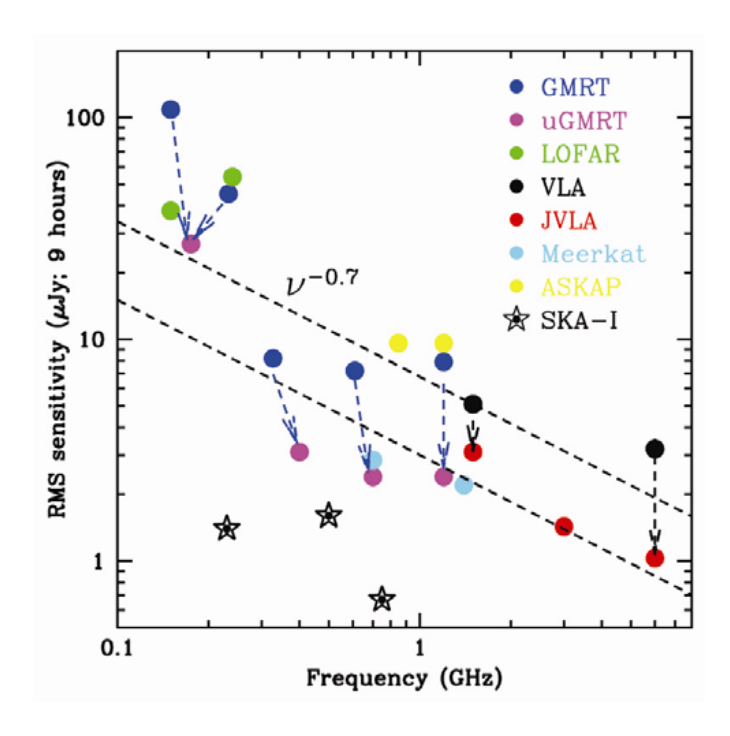


**Figure 1.4:** Comparison of current and planned radio interferometers' continuum sensitivities for a 9-hour on-source integration. The GMRT, VLA, JVLA, uGMRT, LOFAR, MeerKAT, ASKAP, and SKA-1-Mid sensitivities are displayed by the points. As may be observed, until Phase-1 of the SKA is implemented, uGMRT is the world's most sensitive interferometer at frequencies between 250 and 1500 MHz (9).

#### 1.3 Radio Surveys

The advent of highly sensitive radio telescopes has resulted in several large area surveys in the different radio bands. Wide area surveys with very high sensitivities can help uncover different astrophysical processes occurring in various astrophysical sources. They also help investigate how these sources are influenced by their environment. They can also help probe the underlying cosmology driving structure formation and evolution in the Universe (2). The advantages of undertaking radio surveys are faster coverage of large sky areas and the ability to probe high redshift sources (due to lack of dust attenuation). Thus, radio surveys are also crucial for tracing the time evolution of the different source populations. The large population of sources detected by the large areas covered in radio surveys helps in statistical quantification of properties of radio sources—source counts, luminosity functions, clustering, etc. These analyses become helpful in tracing the underlying dark

matter distribution via comparison with simulations.

In the last few decades, the advent of advanced processing techniques and the development of highly sensitive instruments have resulted in many radio surveys by different telescopes. The NVSS and FIRST (3; 4) by VLA at 1.4 GHz and TGSS by GMRT at 150 MHz are a few surveys by the previous generation interferometers. Currently, several large area, high sensitivity surveys are being done, mainly by the new telescopes. They include the LoTSS by LOFAR (5), MIGHTEE by MeerKAT (6), GLEAM by the MWA (7), EMU, RACS, DINGO, etc by ASKAP (8).

However, a few gaps remain despite the existing data for such surveys. The biggest problem is the non-overlap of the sky area covered by telescopes located on opposite hemispheres. For instance, the sky observable by ASKAP is south of  $\delta \sim +40^{\circ}$ , while for LOFAR, the sensitivity drops significantly below  $\delta \sim -5^{\circ}$ . Thus, combining low and high-frequency ends of the radio bands becomes possible for a very small part of the sky. The target fields for surveys are generally chosen such that they have multi-frequency coverage in other frequency bands like optical, IR, X-ray, etc. This helps develop a better understanding of the source characteristics across frequency and time. For instance, optical observations are useful for studying the time evolution of sources through redshift information. Observed luminosities of SFGs in the IR and radio bands show a correlation that is used as a tracer of star formation activities. These are a few examples showing that observed data across different frequencies is key to probe deeper into the underlying processes driving the formation and evolution of different structures in the Universe.

#### 1.4 TIFR GMRT Sky Survey (TGSS)

The Giant Meter-wave Radio Telescope (GMRT) was utilized to map the radio sky at 150 MHz between 2010 and 2012. However, the data products were not initially made publicly accessible. Later, an independent group reprocessed the TGSS data using the SPAM pipeline, which included improvements like corrections for ionospheric phase effects. The revised data and products, collectively referred to as the TGSS Alternate Data Release

(ADR), are now publicly available, with detailed descriptions provided in reference (22).

The TGSS ADR offers several publicly accessible services:

- 1. **TGSS ADR Image Archive**: A collection of 5×5 square degree mosaic images covering the entire survey region.
- 2. TGSS ADR Image Cutout Service: Allows users to retrieve images from any part of the survey region, up to  $1\times1$  square degree in size.
- 3. **TGSS ADR Source Catalogue**: Contains data for 0.63 million radio sources identified across the entire survey area.

The TGSS ADR provides Stokes I continuum images that cover 99.5% of the radio sky above a declination of  $-53^{\circ}$  (approximately 90% of the total sky). The images have a resolution of  $25'' \times 25''$  for the northern sky  $(\delta > 19^{\circ})$  and  $25'' \times 25'' / \cos(\text{Dec} - 19^{\circ})$  for the southern sky  $(\delta < 19^{\circ})$ . The median noise level is 3.5 mJy/beam, and the source catalog includes critical data such as positions, flux densities, and sizes, all derived using a 7-sigma peak-to-noise threshold.

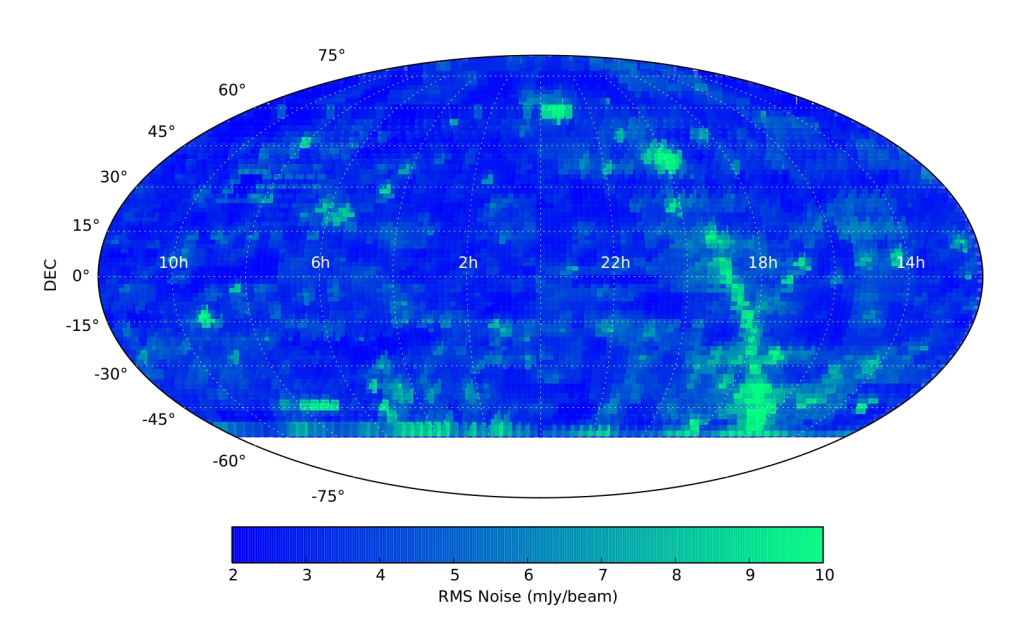


Figure 1.5: RMS noise level map for TGSS in ADR (22).

The upgraded GMRT (uGMRT) significantly enhances the TGSS data in multiple ways due to improvements in hardware, software, and observational capabilities. By utilizing the uGMRT, we can achieve better noise levels, higher resolution, and deeper probing of the sky:

- 1. **Improved Sensitivity**: uGMRT's enhanced receiver systems and wider frequency coverage (100 MHz to 1.5 GHz)(9) improve the sensitivity compared to the legacy GMRT. This allows for the detection of fainter sources and finer details in radio emissions.
- 2. **Increased Bandwidth**: The uGMRT provides a better signal-to-noise ratio (SNR), allowing for clearer images with reduced noise levels. This bandwidth increase will improve the overall quality of TGSS-like surveys by enhancing spectral resolution, which is especially important for observing sources with complex spectral properties.
- 3. **Better Resolution**: The upgraded system enables higher angular resolution by increasing the number of antennas, expanding baselines, and improving frequency coverage. This allows for sharper images, enabling the resolution of smaller and more distant sources that would have been previously unresolved by the legacy GMRT.
- 4. **Deeper Sky Probing**: The increased sensitivity and better resolution of uGMRT will allow for deeper probing of the radio sky, making it possible to detect and study previously undetectable faint sources in the outer reaches of the observable Universe.

While the TGSS ADR has provided valuable insights into the radio sky, the transition to the upgraded GMRT opens up new possibilities for improving the data quality. The uGMRT's enhanced sensitivity, bandwidth, resolution, and calibration techniques will allow for significantly better noise levels, sharper images, and deeper probing of the sky. This means that the next generation of surveys, based on uGMRT data, will provide a more detailed, comprehensive, high-fidelity radio universe map.

## Chapter 2

# Galaxy and Mass Assembly (GAMA) Fields

The Galaxy and Mass Assembly (GAMA) Project (11) is a multi-band imaging and spectroscopic survey of five different fields in the southern sky covering over ~ 286 deg². The main aim of the survey is to study structures on scales 1 kpc to 1 Mpc and test the CDM paradigm of structure formation. The five patches targeted by the GAMA survey—G02, G09, G12, G15, G23, are located between declination range +2° to -35°. The data released from the GAMA project consists of spectra, redshifts, photometry, stellar mass, etc. The GAMA fields are also covered in the radio bands by GMRT (12). Large radio surveys like NVSS, TGSS, GLEAM, etc., also cover GAMA regions. Besides radio, surveys are also present in X-ray, IR, UV, etc. The presence of such a large volume of multi-wavelength data makes the GAMA survey fields the best candidate fields for detailed extragalactic source studies in the southern sky.

#### 2.1 GAMA 23 Field

The GAMA-23 (G23) field is located between  $22h36m00s \le \alpha_{J2000} \le 23h24m00s$  and  $-30^{\circ} \le \delta_{J2000} \le -35^{\circ}$ . It covers a  $\sim 50 \text{ deg}^2$  patch overlapping with the VST ATLAS survey area. Hence, optical data from the Kilo-Degree Survey (KiDS) and VISTA Kilo-degree Infrared Galaxy Survey (VIKINGS) are al-

Region	RA range	Dec range	Main survey limit
G02	30.2 – 38.8	-10.253.72	r < 19.8
G09	129.0 – 141.0	-2-+3	r < 19.8
G12	174.0 – 186.0	-3 - +2	r < 19.8
G15	211.5 – 223.5	-2-+3	r < 19.8
G23	339.0 – 351.0	-35 – -30	i < 19.2

Table 2.1: GAMA survey regions with RA and Dec ranges and main survey limits.

ready available. The availability of data from a diverse range of telescopes at different wavelengths makes the G23 field an excellent candidate for extragalactic studies. G23 is covered by nine different pointings in the TGSS survey, but the images are severely limited in sensitivity. The observation of the G23 region with the uGMRT Band-2 (120-250 MHz) will enhance the sensitivity and will enable us to probe deeper and observe fainter galaxies. The faint end of the cumulative source counts will help better differentiate between various radio source populations. Additionally, it will be useful for studying star formation activity and investigating the evolution of star formation with cosmic time. These observations, in conjunction with data from other wavebands, will thus enable a detailed investigation into the astrophysical processes involved in the formation and evolution of astrophysical source populations.

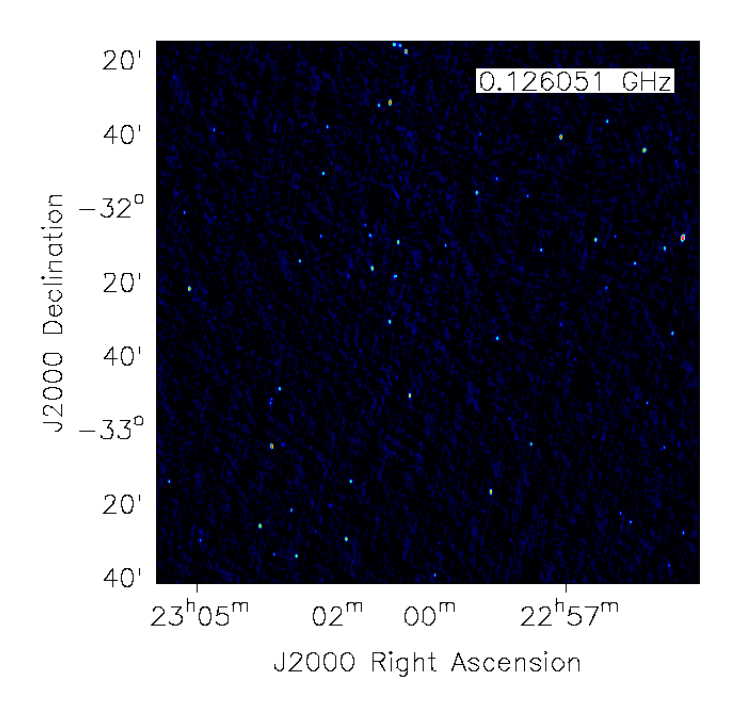


**Figure 2.1:** An image of GAMA 23 field centered at  $\alpha_{J2000} = 23h00m00s$  and  $\delta_{J2000} = -32^{\circ}30'00''$ . This image was obtained from the TGSS Alternative Data Release (22). The off-source RMS noise value is 3.5 mJy/beam.

#### 2.2 Multi-Wavelength Studies of GAMA-23

A multi-wavelength study of the G23 field was conducted (13) at 936 MHz and 1320 MHz using ASKAP. The observation covered an area of approximately 48 deg<sup>2</sup> at 936 MHz with a synthesized beam of 32.7" × 17.8", and 39 deg<sup>2</sup> at 1320 MHz with a synthesized beam of 15.8" × 12.0". At both frequencies, the root-mean-square (r.m.s.) noise was around 0.1 mJy/beam. These radio observations were combined with the GAMA galaxy data to explore the relationship between radio emission and galaxy properties. Additionally, Wide-field Infrared Survey Explorer (WISE) infrared (IR) photometry was utilized to identify galaxies that host an active galactic nucleus (AGN).

Some key conclusions from the study include:

 Out of approximately 5800 radio sources, around 1000 were found to have counterparts in the G23 galaxy catalog, 3000 had WISE IR counterparts, and 900 had both G23 galaxy and WISE IR counterparts. A fraction of the radio sources without WISE counterparts may still host AGN, but these AGN might be too faint to be detected in the IR band. The radio sources associated with G23 galaxies tend to be at the high-mass end of the galaxy distribution, typically with masses greater than  $10^{10}M_{\odot}$  (see Figure 2.2).

 Galaxies detected in the radio band are generally more massive and brighter in the K-band and UV compared to those without radio emission. This suggests that radio emission from AGN is more pronounced in more massive galaxies, which also tend to be brighter in the Kband. Similarly, galaxies with active star formation exhibit stronger radio emission and enhanced UV emission from young stars.

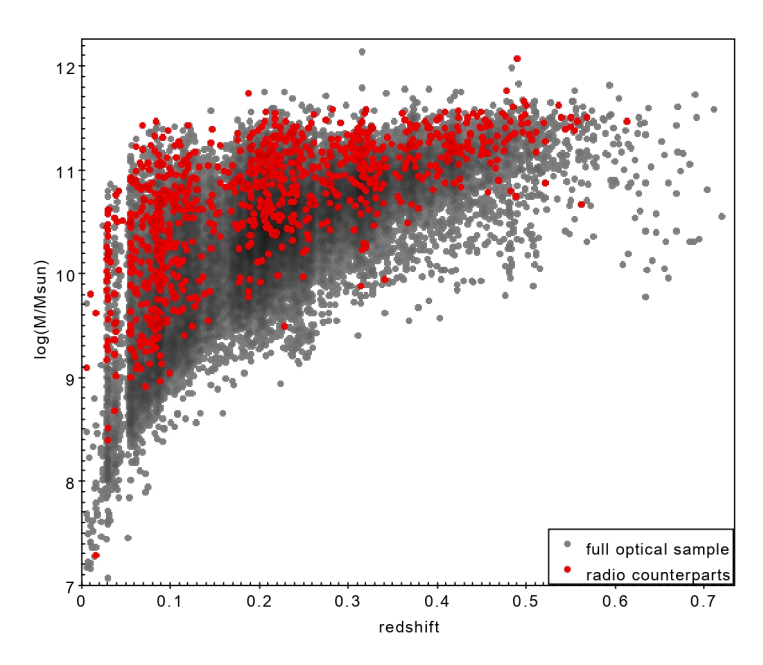


**Figure 2.2:** "Stellar mass in units of  $log(M/M_{\odot})$  vs redshift for the 936 MHz/G23 sources (red), and for all G23 galaxies (grey). This shows that galaxies with detected radio emission are mainly galaxies with larger masses" (13).

Another study was conducted by Quici et al. 2020 (14). The study aimed to identify remnant radio galaxies in the GAMA-23 field using data from multiple radio telescopes spanning frequencies from 0.1 to 9 GHz. It focused on an 8.31 deg<sup>2</sup> subregion of the GAMA-23 field, which offered rich multi-wavelength coverage. The authors compiled data from several telescopes, each contributing unique advantages:

Telescope	Survey	Date observed	Frequency [MHz]	Bandwidth [MHz]	Noise [mJy beam <sup>-1</sup> ]
MWA Phase I	GLEAM SGP	2013–2015	119	30.72	16.2
MWA Phase I	GLEAM SGP	2013–2015	154	30.72	9.3
MWA Phase I	GLEAM SGP	2013–2015	186	30.72	6.7
MWA Phase II	MIDAS ES	2018–2020	216	30.72	0.9
uGMRT	_	2016	399	200	0.1
uGMRT	TGSS	2010–2012	150	32	3.5
ASKAP	EMU-ES	2019	887.5	288	0.035
VLA	NVSS	1993–1996	1400	50	0.45
MeerKAT	MeerHOGS	2019	1416.8	200	0.19
ATCA	GLASS	2016–2020	5500	2000	0.024
ATCA	GLASS	2016–2020	9500	2000	0.04

**Table 2.2:** Summary of properties of the radio surveys covering GAMA-23 (14).

- Low-Frequency Observations (MWA and ASKAP): These were used to detect diffuse, low-brightness lobes.
  - MWA Phase II (216 MHz) provided high sensitivity to large, extended structures.
  - ASKAP EMU-ES (887 MHz) contributed higher resolution for analyzing morphology.
- **High-Frequency Observations (ATCA):** The GLASS survey data (5.5 GHz and 9 GHz) were used to detect compact features and confirm the absence of an active core, which was a key criterion for identifying remnants. Additional low-resolution ATCA observations were conducted to mitigate resolution bias and detect low-surface-brightness emissions.
- Intermediate Frequencies (uGMRT and NVSS): uGMRT (399 MHz) and NVSS (1.4 GHz) filled gaps in the frequency range, enabling detailed spectral modeling.
- Optical/Near-Infrared Data: Host galaxies were matched using the VISTA VIKING near-infrared survey and the GAMA photometry catalog, ensuring accurate host identifications and redshift determinations.

GAMA 23 was also observed using the MeerKAT telescope as part of the MeerHOGS survey at the frequency of 1416.8 MHz, a synthesized beam of 34.4"  $\times$  34.4", and an RMS noise value of 0.19 mJy/beam was achieved (15).

## Chapter 3

# Radio Interferometric Data Analysis

#### 3.1 Measurements from a Radio Interferometer

An interferometer works by sampling the spatial Fourier components of the far-field radiation pattern and then reconstructing the sky's intensity distribution through a Fourier transform. Instead of using a continuous aperture, it employs a discrete set of measurement points (or slits). For each pair of slits, the instrument calculates the interference wavefront's amplitude and phase by correlating the measured electric fields—effectively taking the product of their complex values.

Each pair of slits captures the spatial Fourier transform of the incoming radiation at a specific spatial frequency, determined by their separation in wavelengths. This approach, known as aperture synthesis, allows a sparse array of detectors to mimic a much larger lens aperture—with the effective aperture size defined by the maximum distance between any two slits. Unlike a traditional lens with a continuous aperture, this synthesized aperture consists of a finite number of discrete sampling points, enabling high-resolution imaging through indirect measurement.

To construct a two-dimensional image of the sky, we must measure the power of the radiation field emitted by an object across multiple directions, effectively sampling different regions of the source. A key requirement is that the source must be spatially incoherent, meaning the radiation from one

part of the source is uncorrelated with that from any other part. If the source were spatially coherent, waves from different regions would interfere, and the measured signal would reflect this interference pattern rather than the true intensity distribution.

As radiation propagates from the source to the observer, it becomes partially coherent due to the finite angular size of the source. At large distances, the wavefronts flatten, making it difficult to distinguish emissions from closely spaced points. The van Cittert-Zernike theorem describes this behavior, stating that the spatial coherence of radiation from a distant, spatially incoherent source is proportional to the Fourier transform of the source's intensity distribution. Mathematically, this is expressed as:

$$\langle E_{\nu}(\bar{r}_1)E_{\nu}^*(\bar{r}_1)\rangle \propto \int I_{\nu}(\hat{s})e^{-2\pi i\nu\tau_{12}}d\Omega \equiv V(\bar{r}_1 - \bar{r}_2, \nu)$$
 (3.1)

The electric fields measured at two positions,  $\mathbf{r}_1$  and  $\mathbf{r}_2$ , on the aperture plane are denoted as  $E_{\nu}(\mathbf{r}_1)$  and  $E_{\nu}(\mathbf{r}_2)$ . The **visibility**  $V(\mathbf{r}_1 - \mathbf{r}_2, \nu)$  is defined as the time-averaged cross-correlation of these fields:

$$V(\mathbf{r}_1 - \mathbf{r}_2, \mathbf{v}) = \langle E_{\mathbf{v}}(\mathbf{r}_1) E_{\mathbf{v}}^*(\mathbf{r}_2) \rangle, \tag{3.2}$$

where  $\langle \cdot \rangle$  represents the time average and \* denotes complex conjugation. The visibility is a complex quantity that depends only on the **baseline vector**  $\mathbf{b} = \mathbf{r}_1 - \mathbf{r}_2$  (the separation between detectors in wavelengths), and not on their absolute positions. Here,  $d\Omega$  represents the differential solid angle subtended by the source on the celestial sphere.

#### 3.1.1 Coordinate systems

Visibilities represent the measured correlations from multiple detector pairs at frequency v. These measurements are combined to reconstruct the intensity distribution at that frequency. The imaging process requires defining coordinate systems that relate the sky brightness to the synthesized aperture and detector positions.

Let  $\hat{X}\hat{Y}\hat{Z}$  denote the terrestrial coordinate system for antenna locations. The phase-reference center  $\hat{s}_0$  (pointing direction) is specified by declination  $\delta_0$  and hour-angle H.

The sky brightness distribution  $I_{\nu}(\hat{s})$  is described in  $\hat{l}\hat{m}\hat{n}$  coordinates, where l,m,n are direction cosines. The phase center corresponds to  $\bar{s}_0(0,0,1)$ , with off-center points as  $\hat{s} = \hat{s}_0 + \hat{s}_{\sigma}$ . The resulting 2D image projects this distribution onto the  $\hat{l}\hat{m}$  tangent plane at  $\bar{s}_0$ .

The aperture plane  $(\hat{U}\hat{V})$  is perpendicular to  $\hat{s}_0$  (aligned with  $\hat{W}$ ). The  $\hat{U}\hat{V}\hat{W}$  system relates to  $\hat{X}\hat{Y}\hat{Z}$  through:

$$\begin{bmatrix} u \\ v \\ w \end{bmatrix} = \frac{1}{\lambda} \begin{bmatrix} \sin H & \cos H & 0 \\ -\sin \delta_0 \cos H & \sin \delta_0 \sin H & \cos \delta_0 \\ \cos \delta_0 \cos H & -\cos \delta_0 \sin H & \sin \delta_0 \end{bmatrix} \begin{bmatrix} x \\ y \\ z \end{bmatrix}$$
(3.3)

Here (x, y, z) are physical coordinates (meters), while (u, v, w) are wavelength-scaled  $(\lambda = v/c)$ . Earth rotation causes (u, v) coordinates to trace elliptical paths. Baseline vectors  $\vec{b}(u, v, w) = \vec{r}_1 - \vec{r}_2$  connect detector positions  $\vec{r}_i(u_i, v_i, w_i)$ , with components:  $u = u_1 - u_2$ ,  $v = v_1 - v_2$ ,  $w = w_1 - w_2$ .

Since detectors may lie off the aperture plane  $(w_i \neq 0)$ , the wavefront arrival time difference between detectors is:  $\tau = \vec{b} \cdot \hat{s}_0/v = (w_1 - w_2)/v$ , which must be corrected prior to correlation.

#### 3.1.2 Delayed correction

Delay correction aligns signals from each detector so that, at any moment, all detectors sample the wavefront at the aperture plane rather than their physical positions.

The delay for the detector at  $\vec{r}_1$  equals the signal travel time across  $\vec{r}_1 \cdot \hat{s}_0 = w_1$ . When  $\delta_0 = 90$ ,  $w_1 = w_2 = 0$ , so both detectors  $\vec{r}_1$ ,  $\vec{r}_2$  sample the same wavefront. For  $\delta_0 \neq 90$ ,  $w_1$  and  $w_2$  typically differ, and  $\vec{r}_1$ ,  $\vec{r}_2$  sample the wavefront with time delays  $\tau_1^c = w_1/v$  and  $\tau_2^c = w_2/v$  relative to the coordinate origin. Correcting these delays involves sending  $E(\vec{r}_1, t - \tau_1^c)$  and  $E(\vec{r}_2, t - \tau_2^c)$  to the correlator. As Earth rotates, continuous correction keeps the aperture fixed on  $\hat{s}_0$ . For an EM-wave from  $\hat{s} = \hat{s}_0 + \hat{s}_\sigma$ , the residual delay after correction is:

$$\tau_{12} = \vec{b} \cdot (\hat{s} - \hat{s}_0) / v = (ul + vm + w(n-1)) / v \tag{3.4}$$

This time delay corresponds to  $\tau_{12}$  in Eq. 3.1, introducing a phase term in the measured complex visibility.

#### 3.2 Imaging

The relation in Eq. 3.1 for a celestial sphere source  $d\Omega = \frac{dl \, dm}{n}$  becomes:

$$V(u, v, w) = \iint \frac{I(l, m, n)}{n} e^{-2\pi i(ul + vm + w(n-1))} dl dm$$
 (3.5)

Here, l and m are direction cosines representing coordinates on the tangent plane at  $\hat{s}_0$ . For a sky position  $\hat{s} = \hat{s}_0 + \hat{s}_\sigma$ , the term (n-1) accounts for the distance between the true curved sky and the tangent plane approximation at  $\hat{s}_0$ . The product w(n-1) represents the w-term, which quantifies the phase difference due to sky curvature between detectors forming baseline  $\vec{b}$ . When  $w(n-1) \neq 0$ , even after delay correction, detectors sample different wavefront phases, with  $e^{-2\pi i w(n-1)}$  acting as a Fresnel propagation kernel compensating for the  $\lambda w(n-1)$  path difference.

For imaging regions near the phase center ( $n \approx 1$ ), the *w*-term becomes negligible, reducing Eq. 3.5 to a 2D Fourier transform relation between mutual coherence and source brightness:

$$V(u,v) = \iint I(l,m)e^{-2\pi i(ul+vm)}dl\,dm \qquad (3.6)$$

This fundamental result, known as the van Cittert-Zernike theorem, defines the visibility function as the 2D Fourier transform of the brightness distribution. Each baseline measures one complex-valued sample of this function in the *uv*-plane, characterizing the interference fringe pattern.

With complete *uv*-coverage, the brightness distribution could be recovered through the inverse Fourier transform:

$$I(l,m) = \iint V(u,v)e^{2\pi i(ul+vm)}du\,dv \tag{3.7}$$

However, practical interferometers provide only discrete sampling. For  $N_a$  antennas, the  $N_a(N_a-1)/2$  baselines simultaneously measure spatial frequencies determined by projections of  $\vec{b}(u,v,w)$ . This sampling pattern defines the array's transfer function:

$$S(u,v) = \sum_{k=1}^{N_b} \delta(u - u_k) \delta(v - v_k)$$
(3.8)

where  $N_b$  is the number of unique baselines.

where k is an index denoting a measurement from a single baseline, the spatial frequency plane can be additionally sampled by adjusting antenna positions relative to the phase-reference center. For ground-based arrays, Earth's rotation causes all projected baseline vectors  $\dot{b}_{\hat{s}_0}$  to trace elliptical paths on the spatial frequency plane, gradually filling it. This technique is called Earth Rotation Aperture Synthesis. As measured spatial frequencies are expressed in wavelength units, observations at multiple frequencies enhance spatial-frequency plane sampling, a method known as Multi-Frequency Aperture Synthesis. Because spatial frequency measurements vary with time and observing frequency, data must be acquired with adequate time and spectral resolution to avoid visibility averaging (smearing) in the spatial frequency domain. This typically produces a uv-plane sampling pattern dominated by central concentrations, featuring a central gap and diminishing outer edges. Here, S(u,v) represents the complete set of sampled spatial frequencies (discretized across baselines, time, and frequency). The sampling function or uv-coverage S(u, v) determines the imaging characteristics of the synthesis array. The highest measured spatial frequency sets the instrument's angular resolution, while the lowest determines its maximum detectable spatial scale. The sampling density within this range governs the array's inherent sensitivity to different spatial structures.

For an interferometric array with specified uv-coverage, the image produced by Fourier transforming measured visibilities can be characterized as follows. The measurement process multiplies the true visibility function (representing sky brightness) by the instrument's uv-coverage. The observed visibility becomes  $V_{\rm obs}(u,v) = S(u,v)V(u,v)$ , and the image formed through direct Fourier inversion of measurements is expressed as

$$I^{\text{obs}}(l,m) = \iint S(u,v)V(u,v)e^{-2\pi i(ul+vm)}dudv$$
 (3.9)

Per the Fourier convolution theorem, the unprocessed or dirty image  $I^{\rm dirty}(l,m)$  consequently results from convolving the actual sky brightness I(l,m) with the instrument's point spread function  $I^{\rm psf}(l,m)$ , obtained as the Fourier transform of the uv-coverage.

$$I^{\text{obs}} = I * I^{\text{psf}} \tag{3.10}$$

where

$$I^{\mathrm{psf}}(l,m) = \iint S(u,v)e^{2\pi i(ul+vm)}du\,dv,\tag{3.11}$$

Here, \* signifies convolution, and the point spread function characterizes the instrument's response to a unit-brightness point source at the phase center (V(u,v)=1). This represents the image generated when monochromatic plane wave radiation arrives from a single sky direction. As the observed image is a convolution of sky brightness with a known instrumental response, the true sky brightness distribution can be estimated through deconvolution techniques.

#### 3.3 Calibration

In practice, the visibility measurement equation is adjusted to include antennabased complex gain factors  $\hat{a}_i$ , which may vary with time, frequency, antenna position, and observing direction. Accounting for these gains, the measurement equation becomes:

$$V_{ij}(u,v,w) = \iint a_i(l,m)a_j^*(l,m)\frac{I(l,m,n)}{n}e^{-2\pi i(u_{ij}l+v_{ij}m+w_{ij}(n-1))}dldm,$$
(3.12)

where  $V_{ij}(u, v, w)$  represents the visibility function for a baseline formed by antennas i and j. Estimating these gain factors is known as *calibration*. To reconstruct an accurate sky brightness distribution, measured visibilities must first be calibrated to correct for instrumental distortions. Calibration involves first determining the  $a_i$  terms using observations of a source with a known structure, then applying these solutions to remove directionindependent gain effects from the target source's visibilities.

#### 3.3.1 Gain Solution

For an observed visibility  $V_{ij}^{\text{obs}}$  between two antennas, the calibration equation is expressed as:

$$V_{ij}^{\text{obs}} = a_i a_j^* V_{ij}^{\text{model}}, \tag{3.13}$$

Where  $V_{ij}^{\text{model}}$  is the visibility derived from a known source model  $\bar{I}^{\text{model}}$ , obtained by computing its spatial Fourier transform and sampling it using S(u,v). A weighted least-squares solution (24) is obtained by minimizing:

$$\chi^2 = \sum w_{ij} \left| V_{ij}^{\text{obs}} - a_i a_j^* V_{ij}^{\text{model}} \right|^2, \tag{3.14}$$

which directly estimates the antenna-based complex gains. Here,  $w_{ij}$  denotes the visibility weight, given by the inverse noise variance. The gain corrections for all baselines are derived from the antenna-based solutions and applied to calibrate the observed visibilities. Note that this formulation assumes the gain factors are direction-independent.

#### 3.3.2 Standard Calibration

In standard calibration procedures, observations of astronomical sources with known properties are interleaved with observations of the target source. These calibrator observations provide reference measurements from which antenna-based gain solutions can be derived for specific time intervals. The solutions are then interpolated to the times when the science target was observed and applied to correct its visibilities (23).

The gain solution process typically separates amplitude and phase corrections. Bright, stable sources serve as *flux calibrators* to determine gain amplitudes, while sources with precisely known positions act as *phase calibrators* to solve for phase variations. The ideal calibrators are point-like sources exhibiting constant visibility across all measured spatial frequencies, though extended sources with well-characterized structures can also be employed.

Bandpass calibrators, consisting of sources with flat or well-understood spectral characteristics, are used to measure frequency-dependent gain variations. To enhance the signal-to-noise ratio for the gain solutions, visibility data may be averaged along axes where the solutions are expected to remain stable. For instance, bandpass calibration frequently employs time-averaged data since the frequency response typically remains constant over certain time periods. Subsequent calibration steps address time-variable effects using these bandpass-corrected measurements, now averaged in frequency to produce single values per time interval.

#### 3.3.3 Self Calibration

Since gain solutions for the target source are computed through interpolation between calibrator scans, any gain variations during target observation remain unaccounted for. *Self-calibration* solves this by using the target source itself as a calibrator, deriving gain solutions from a model of the source. This model may come from prior knowledge (such as an existing image) or be constructed iteratively from the observed data.

In principle, self-calibration (24; 25) is an iterative cycle of calibration and imaging. It performs  $\chi^2$  minimization in two alternating stages: first optimizing the sky model  $\bar{I}_{sky}$ , then solving for the antenna gains  $[a_i$ 's], while applying appropriate physical constraints to each.

When a high-fidelity initial sky model exists, self-calibration often converges in one iteration. The specific parameters solved for depend on external calibrator availability:

- After standard flux calibration using an external source, phase-only self-calibration can further refine the solutions.
- For full amplitude-and-phase calibration, where the model and target amplitudes differ, the gain solutions are normalized to preserve the overall flux scale.

Without prior source information or external calibrators, the process begins with a unit-flux point source model at the phase center and unity antenna gains. Multiple iterations are typically needed for convergence, though absolute position and flux information may be absorbed into the gains and lost during correction. This method works best for sources with a simple spatial structure.

#### 3.3.4 Direction Dependent Calibration

The calibration approach described above is typically called *direction-independent* calibration, as it assumes each antenna's gain solution applies uniformly across the entire observed sky. This implies the  $a_{0i}$  terms in Eqn. 3.10 are treated as direction-independent. However, at low frequencies, this assumption frequently breaks down due to: (1) primary beam variations across

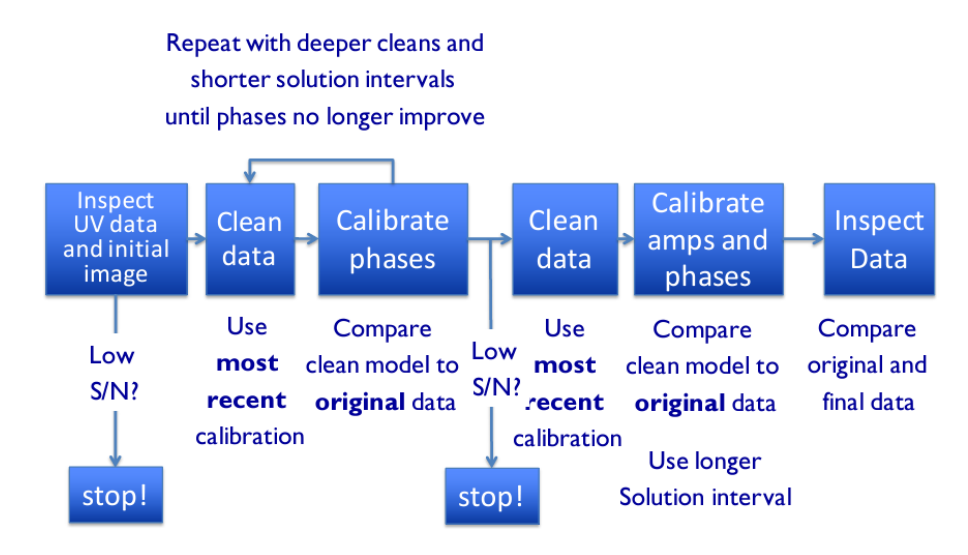


Figure 3.1: Steps taken during self-calibration. Credit: NRAO

wide fields of view, (2) frequency-dependent effects, and (3) ionospheric distortions that vary with position and time (26). These effects necessitate direction-dependent solutions for the gain terms in Eqn. 3.10.

Precise direction-independent and direction-dependent calibration is critical for 21 cm observations, particularly before any definitive detection, and represents a major focus of current research. The observed sky brightness couples with the time- and frequency-varying primary beam, requiring careful separation of intrinsic sky signals from beam effects. Due to rapidly changing sidelobe patterns, primary beam variations are most pronounced away from the pointing center. While the main beam scales smoothly with wavelength, sidelobe regions exhibit abrupt variations—a source may lie on a sidelobe peak at one frequency and a null at another. Inaccurate beam modeling distorts calibration solutions and disrupts foreground frequency smoothness.

Ionospheric effects present additional low-frequency challenges. This partially ionized atmospheric layer (50–1000 km altitude) introduces propagation delays proportional to its time-varying electron density. Being inherently direction-dependent, ionospheric distortions require direction-dependent calibration strategies. The *peeling* technique addresses this by performing self-calibration on individual bright sources sequentially—calibrating, subtracting, and replacing each source with a model before proceeding to the next. Peeling can target all prominent sources or focus selectively on those

deviating significantly from global solutions, partially accounting for directional gain variations through discrete directional solutions.

#### 3.4 Data reduction using SPAM

The Peeling and Atmospheric Modeling (SPAM) pipeline was used to calibrate the data. SPAM is a fully automated pipeline based on the Astronomical Image Processing System (AIPS) (17). It uses the ParselTongue interface to access AIPS task and files (21). It can do both direction-independent and direction-dependent calibration. It employs a direction-dependent approach to iteratively solve for ionospheric phase corrections, thereby addressing ionospheric phase errors. These errors are likely to persist due to the low observing frequencies of the current dataset. By modeling and correcting for ionospheric dispersive delays, SPAM enhances both the background noise levels and the accuracy of the flux scale.

A brief overview of the data reduction process is provided below:

- 1. **Pre-processing:** SPAM initiates by executing instrumental calibration with the optimal scan of the primary calibrator, subsequently applying these solutions to calibrate the data. The flux densities of the primary calibrators are determined according to the flux density scale. Subsequent to the preliminary RFI identification and the elimination of erroneous data, both time-dependent complex gain solutions and time-independent bandpass solutions are calculated for each antenna and polarization. Furthermore, at this point, the data is temporally and spectrally averaged to diminish its volume, hence streamlining later calibration processes.
- 2. **Direction Independent Calibration:** This is similar to self calibration. It employs a sky model to execute self-calibration on the data. The calibrated visibilities are imaged with wide-field imaging with Briggs weighting and a robust parameter of -1.
- 3. **Direction-Dependent Calibration:** The gain phases and sky model from the previous step serve as inputs for initiating direction-dependent calibration. SPAM determines the gain phases by isolating the bright

sources within the field, known as peeling. The resulting phase correction factors quantify the ionospheric phase delays, which are then applied to the previously calibrated data. This process produces visibility corrected for ionospheric phases. At the end of this, the primary beam-corrected image is obtained.

SPAM can not accommodate the processing of extensive fractional bandwidths  $(df/f \gtrsim 0.2)$  in a single execution; rather, the bandwidth may be divided into smaller segments (sub-bands) that can be processed independently. When executed individually, the calibrated output visibilities from the SPAM pipeline across numerous sub-bands can be collectively imaged using a wideband imager (WSClean) as a concluding procedure.

The following are the steps for using SPAM for wideband:

- 1. The wideband data is split into smaller frequency chunks (subbands). The width of the frequency segments is automatically configured to an appropriate value.
- 2. Each frequency segment is processed independently, analogous to narrow-band GMRT observations. Subsequently, the data undergoes pre-calibration. A constant reference frequency is established to provide uniform frequency averaging across all frequency segments, which is crucial for the subsequent joint imaging of the SPAM output visibilities.
- 3. After that, the main SPAM pipeline is used. A singular reference sky model is employed for all simulations. The reference model is derived by initially executing SPAM on the narrow-band GMRT (GSB) data collected concurrently with the uGMRT wideband data and subsequently extracting a sky model from the resultant image.
- 4. Each SPAM pipeline execution on a sub-band produced a final image and a calibrated visibility dataset. The calibrated sub-band visibility data is transformed into measurement sets with CASA. Subsequently, WSClean is employed to do a last wideband imaging.

### 3.5 uGMRT Observation

The uGMRT data we are working on is a single 9 hours pointing at the G23 field centered at  $\alpha_{J2000} = 23h00m00s$  and  $\delta_{J2000} = -32^{\circ}30'00''$ , at the frequency of 150 MHz. The data contains data from both the legacy GMRT software end (GSB) and the upgraded GMRT wideband backend (GWB). Further observational details are provided in Table 3.1.

Due to the equatorial position of GMRT and the source's southern position, the telescope's pointing is horizontal, which introduces high levels of RFI (Radio Frequency Interference) from terrestrial sources and atmospheric attenuation due to the low elevation. Mitigating this RFI and data calibration is a substantial part of the work.

Parameters	GMRT Wideband Backend (GWB)		
Project Code	42_034		
Observation Date	18 July 2022		
Working Antennas	29		
Usable Bandwidth	100 MHz		
Number of Channels	16384		
Integration Time	8 secs		
Frequency Resolution	16 kHz		
Total Observation Time	9 hours		
Flux Calibrator	3C286 & 3C48		
Phase Calibrator	2321-163		

Table 3.1: Observation summary for GWB data.

# **Chapter 4**

# **Discussions and Results**

## 4.1 Data analysis

We initially attempted to process the GSB data using SPAM. However, SPAM was unable to handle the data, likely due to the significant levels of RFI resulting from the horizontal pointing of the telescope. Consequently, we shifted our focus to the GWB data. The UV coverage of the GWB data before calibration is presented in Fig. 4.1, highlighting the spatial frequency sampling achieved by the array configuration during the observation.

SPAM is not designed to process datasets with extensive fractional bandwidths  $(df/f \gtrsim 0.2)$  in a single run. Therefore, the data was divided into 12 sub-bands over a two-week period of continuous processing. Sub-bands outside Band 2 of the uGMRT were excluded, leaving seven sub-bands within the frequency range of 120–250 MHz for further analysis.

A reference frequency of 150 MHz was chosen to ensure uniform frequency averaging across all sub-bands, a critical step for coherently imaging the SPAM-calibrated visibilities. Each sub-band was pre-calibrated individually before applying the main SPAM pipeline. Given the inaccessibility of the GSB data, a sky model derived from the TGSS survey was used as the reference model for calibration.

During the main pipeline run, the data undergoes multiple iterations of imaging, which is used for self-calibration. With each iteration, the quality of the images improves, refining the calibration process. After a successful run, the pipeline produces a final image and a calibrated visibility dataset.

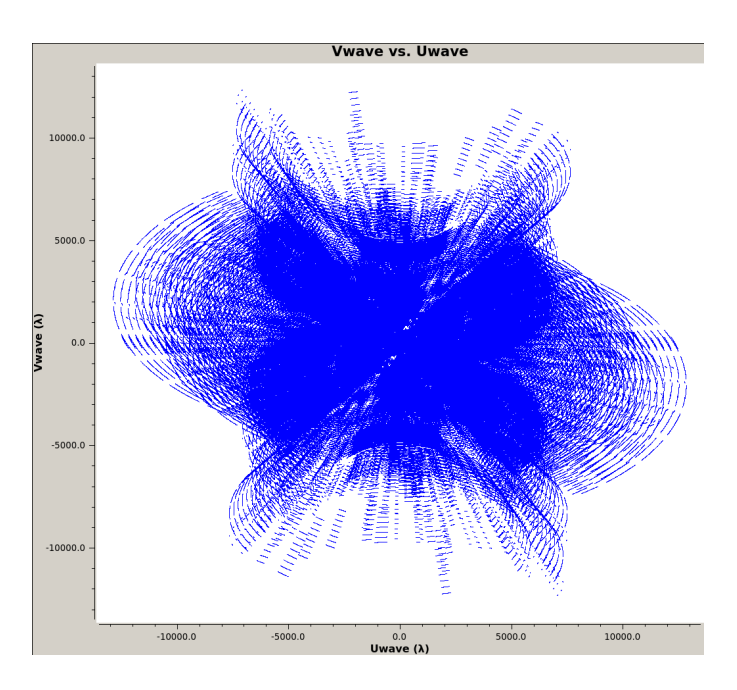
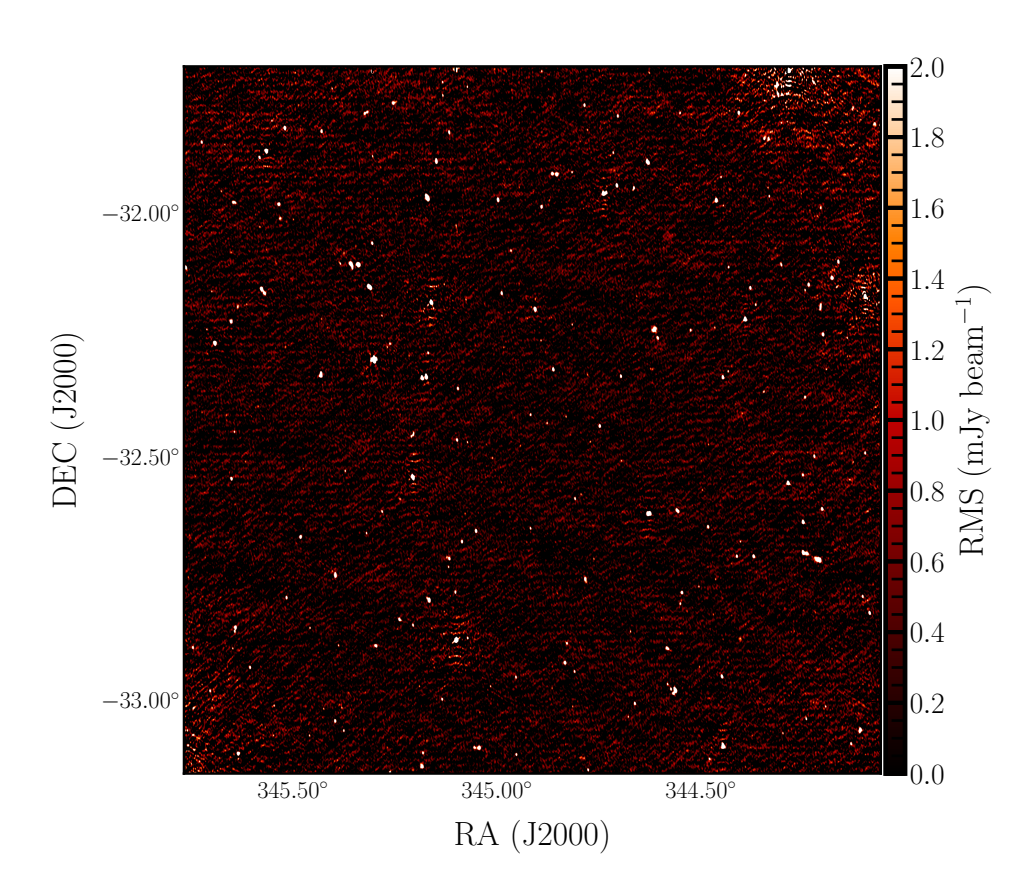


Figure 4.1: UV coverage of the dataset before applying calibration.

After calibrating all sub-bands, calibrated visibilities were used for wide-field imaging using WSClean (18) (Fig. 4.2). An off-source RMS noise value of 316  $\mu$ Jy/beam and a resolution of 15.35"×8.22", which is caused by the poor uv coverage along the v axis, which in turn is due to the low declination of our phase center.

By comparing Figures 2.1 and 4.2, which cover the same RA-Dec region, it is evident that the number of visible sources is significantly higher in Figure 4.2 compared to the TGSS survey. Additionally, the resolution in Figure 4.2 is markedly improved, allowing for finer details to be resolved.



**Figure 4.2:** The final wideband image of the GAMA 23 field. The Flux density is in the unit of Jansky per beam. The off-source RMS noise value is  $316 \,\mu Jy/beam$ , and the resolution is  $15.35"\times8.22"$ .

## 4.2 Comparison with other Radio Catalogs

The image obtained from the band 2 data was compared and cross-examined with other radio catalogs. The GAMA 23 field has been studied at various frequencies, such as the Survey University Molonglo Sky Survey (SUMSS) (27) at 843 MHz, the GaLactic and Extragalactic All-sky MWA survey (GLEAM) (28) at 130 MHz, the NRAO VLA Sky Survey at 1400 MHz, the Rapid ASKAP Continuum Survey at 943.5 MHz (30), and the TGSS (22) at 150 MHz.

Cross-examining the source catalog with prior studies is essential due to pronounced ionospheric fluctuations at low frequencies, which can distort source positions and cause smearing effects for sources far from the phase center. We can quantify systematic offsets in flux densities and source positions by comparing with existing catalogs.

Using a 5" search radius, counterparts of the sources in our catalog were identified in other catalogs. Each reference catalog has a flux density limit determined by observational sensitivity and completeness. Only sources with flux densities exceeding this threshold were selected.

Table 4.1 summarizes the resolution, frequency, and flux limits, values for each catalog used in this analysis.

Survey	Telescope	Frequency	Resolution	Survey Flux
				density limit (mJy)
GLEAM	MWA	130 MHz	130"	50
NVSS	VLA	1400 MHz	45"	2
RACS	ASKAP	943.5 MHz	11.8"	2.5
SUMSS	Molonglo Radio Telescope	843 MHz	45"	10
TGSS	GMRT	150 MHz	40"	30

**Table 4.1:** Comparison of radio surveys with their telescope, frequency, resolution, and noise levels.

## **4.2.1** Flux Density Offset

Different radio source catalogs adopt varying flux calibration scales. In this work, the Scaife-Heald scale (31) has been applied for flux density calibra-

tion, consistent with the TGSS. In contrast, other datasets such as the RACS survey (32), the GLEAM survey (33), and the NVSS and SUMSS utilize the Baars et al. (34) flux scale. Due to differences in calibration schemes and uncertainties in primary beam modeling, minor systematic deviations in the flux densities may occur. To evaluate potential offsets, flux densities of sources from this work were compared with those listed in the aforementioned catalogs. Following the criteria outlined in Williams W. L., et al.(40), only high signal-to-noise ratio (SNR) sources with peak flux densities  $S_{\text{peak}} > 10\sigma$  were selected for this comparison.

To ensure a fair comparison, only compact sources—i.e., sources with sizes smaller than the resolution limit at higher frequencies—were included. An additional flux density threshold was also imposed, based on the limits defined in each catalog. For example, the TGSS catalog applies a flux limit of 30 mJy. Only sources above these flux limits (listed in Table 4.1) were selected for further analysis.

Flux density ratios were computed by appropriately scaling the fluxes from each catalog and calculating  $S_{183\mathrm{MHz}}/S_{\mathrm{others}}$ , where  $S_{\mathrm{others}}$  denotes the flux from the external catalogs. The median ratio obtained with respect to the TGSS catalog is 1.18, with a standard deviation of 0.43. For other catalogs such as NVSS, GLEAM, SUMSS, and RACS, the respective median ratios were found to be 0.85, 1.3, 0.93, and 1.01. These values, shown in Figure 4.3, indicate that the fluxes are consistent across catalogs, generally clustering around unity, which supports the reliability of the flux measurements.

To further test the consistency of the flux scale, sources common to the RACS catalog, the NVSS catalogue, and the present work were identified using the same selection criteria. Spectral indices were estimated from flux densities in the two external catalogs, yielding an average spectral index of 0.73. This value was used to compute expected fluxes at 183 MHz, which were then compared to the fluxes in the present catalog. The resulting flux ratios have a median of 1.03 with a standard deviation of 0.33, as illustrated in Figure 4.4. These results confirm that the adopted flux scale is reasonably accurate for the sources used in this study.

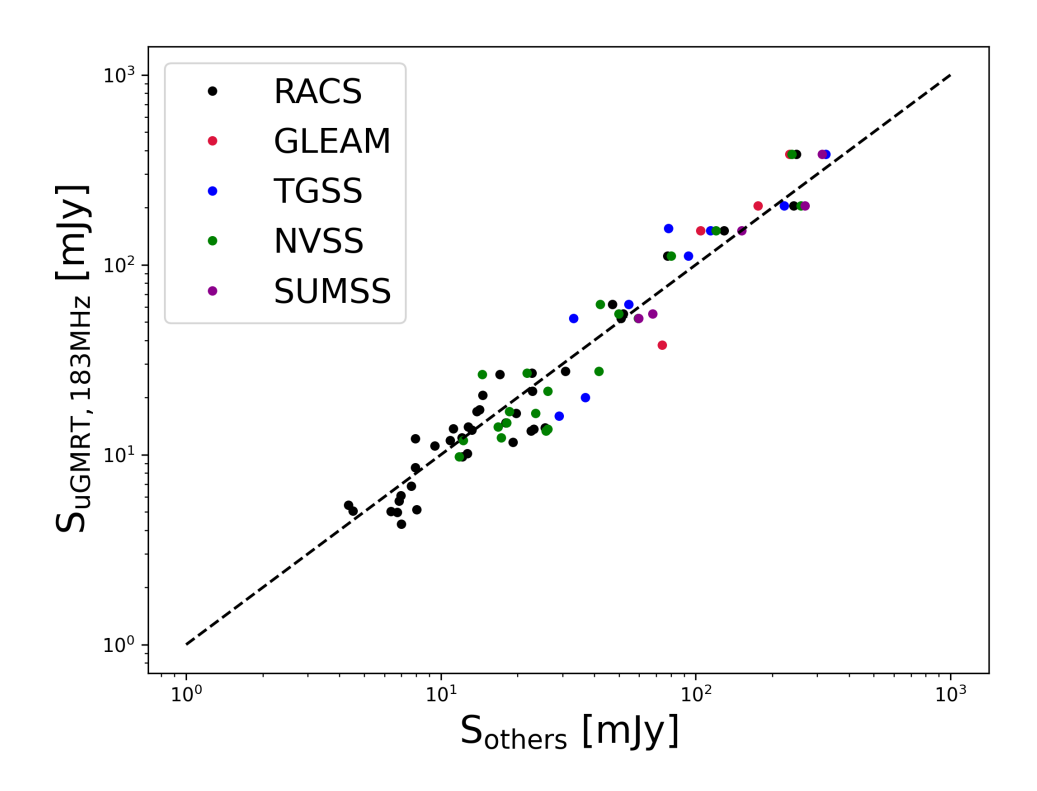


**Figure 4.3:** The compared flux densities of the GAMA-23 band image at 183 MHz with other catalogs.

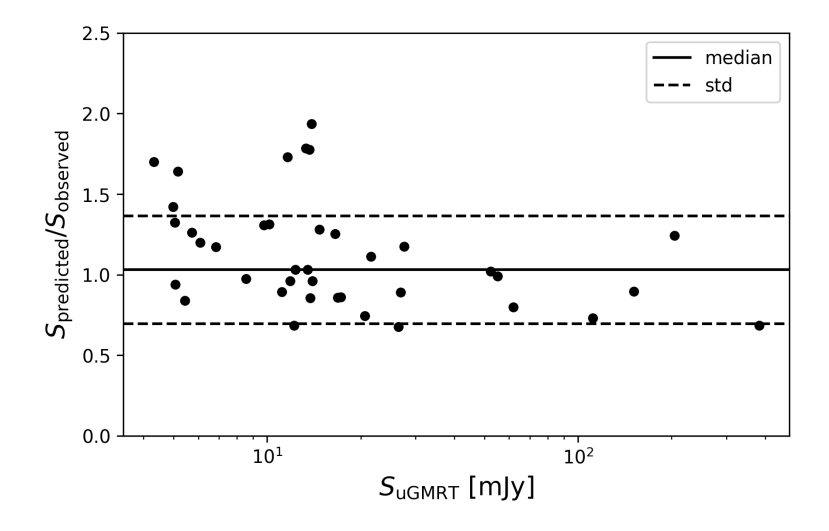


**Figure 4.4:** Comparison of predicted and observed flux densities at 183 MHz. The predicted fluxes are derived using a spectral index 0.73 estimated from RACS and NVSS catalogues.

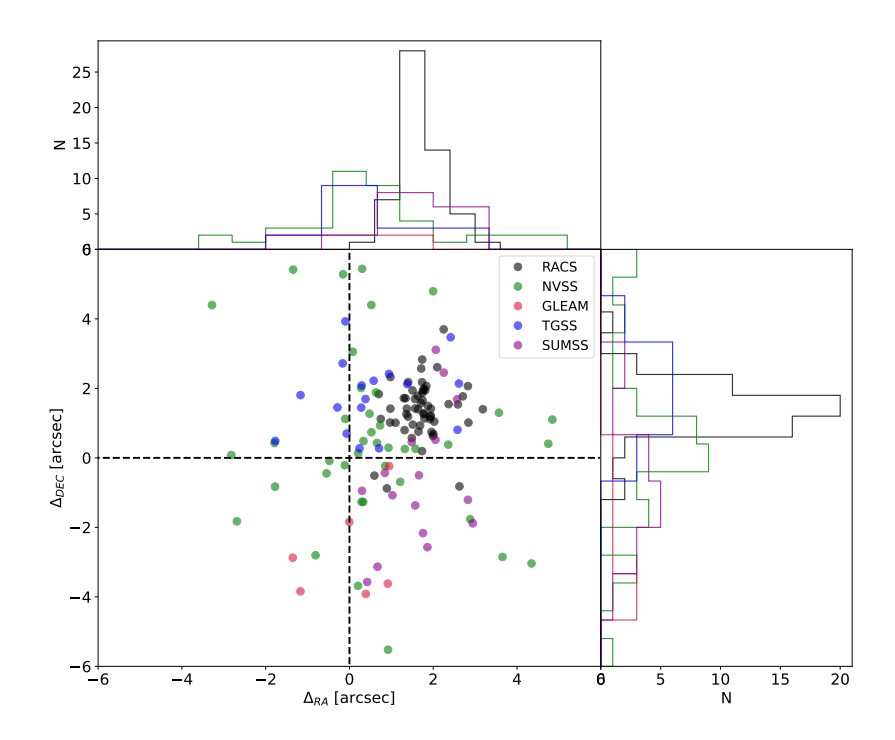


**Figure 4.5:** Offset of the source RA and Dec for the 183 MHz catalog from different catalogs.

### 4.2.2 Positional Accuracy

A positional comparison was conducted with sources from the NVSS, RACS, SUMSS, GLEAM, and TGSS source positions to assess the astrometric accuracy of the current catalog. The positional offsets were calculated as per the method outlined in Williams W. L., et al.(40), using the following relations:

$$\Delta RA = RA_{uGMRT183} - RA_{RACS} \tag{4.1}$$

$$\Delta DEC = DEC_{uGMRT183} - DEC_{RACS}$$
 (4.2)

The median offset values, along with their respective uncertainties, are provided in Table 4.2. Figure 4.5 shows histograms of the positional offsets when compared to the other catalogues. No systematic trends across the field were detected. Furthermore, the observed offsets are smaller than the image cell size (2.5"), indicating that any astrometric error introduced is negligible.

Catalogue	Frequency (MHz)	ΔRA (arcsec)	ΔDEC (arcsec)
RACS	943.5	$1.735 \pm 0.530$	$1.416 \pm 0.792$
NVSS	1400.0	$0.407 \pm 1.868$	$0.337 \pm 2.472$
GLEAM	130.0	$0.193\pm0.920$	$-3.246 \pm 1.319$
TGSS	150.0	$0.291 \pm 1.171$	$1.805 \pm 1.024$
SUMSS	843.0	$1.707 \pm 0.791$	$-1.012 \pm 1.857$

**Table 4.2:** Median astrometric offsets of the uGMRT 183 catalogue relative to RACS and NVSS, along with their respective central frequencies.

### **4.2.3** Spectral Index Distribution

The GAMA-23 field incorporates a diverse population of radio sources. To investigate their spectral characteristics, we compared flux measurements from this study with the RACS catalog. Following the source selection methodology outlined in Section 4.2.

Using a standard synchrotron power-law model  $(S_v \propto v^\alpha)$ , we calculated spectral indices  $(\alpha)$  for the matched sources. Fig. 4.6 presents the resulting distribution, showing peak normalized counts in the  $\alpha$  range of approximately -1.0 to -0.5. Our analysis yields median spectral indices of -0.63, suggesting a characteristic value of  $\alpha \approx -0.7$  for this catalog. These results align with a previous study of the GAMA-23 region, Leahy et al. 2019 (13).

## 4.3 Source Count

This section presents the differential source counts derived from the flux densities obtained through PYBDSF processing. At low radio frequencies, the faint end of the flux distribution is predominantly populated by star-forming galaxies (SFGs) and radio-quiet quasars (RQQs). This trend is supported by both observational studies and simulations (e.g., Wilman et al. 2008 (36); Bonaldi et al. 2018 (37)). Despite this, the number of observational studies that probe sub-mJy populations remains limited.

For instruments like the MWA, LOFAR, and the upcoming SKA, designed to detect the cosmological 21-cm HI signal, these faint sources serve as foreground contaminants that may hinder the detection of the desired

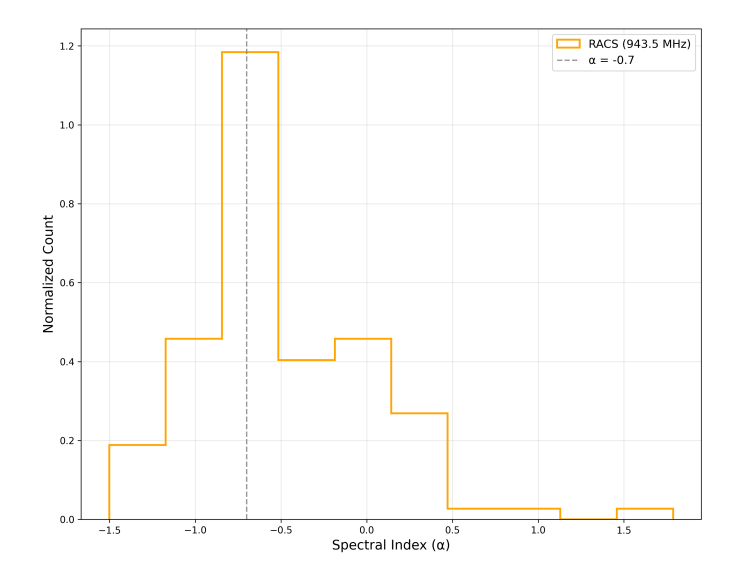


**Figure 4.6:** Normalized distribution of spectral index measurements in the field, obtained by cross-matching with RACS using a 5" matching radius. The black dashed line indicates a spectral index of -0.7.

signal. As such, it is crucial to understand both the spatial and spectral characteristics of radio sources in the sub-mJy to  $\mu$ Jy regime, particularly at low frequencies. A key step in this process is the construction of accurate source counts, which quantify how sources are distributed across different flux densities.

In this work, differential source counts at 183 MHz were computed for sources with flux densities as low as 0.2 mJy (roughly  $4\sigma$ ). However, these raw counts do not represent the true distribution due to several biases and limitations in the PYBDSF output, such as catalog incompleteness, resolution effects, false detections, and Eddington bias. These issues are especially pronounced at low frequencies and for faint sources. The next subsections outline the corrections applied to mitigate these effects and obtain a more reliable estimate of the source counts.

### **4.3.1** False Detection Rate

False detections refer to false sources mistakenly identified by the source extraction algorithm, typically arising from random noise fluctuations or residual artifacts near bright sources in the image. When the noise in the image is symmetrically distributed about zero, the number of positive noise

peaks (which can appear as false sources) should be approximately equal to the number of negative peaks.

To estimate the False Detection Rate (FDR), the source finder PYBDSF was executed on an inverted version of the image, using the same detection parameters as applied to the original.

To correct the FDR across different flux density bins, the negative sources detected in the inverted image were binned in the same way as the real sources. These were then compared to the number of detections in the corresponding bins of the original image. The fraction of real sources in each bin,  $f_{\text{real},i}$ , was calculated following the prescription of Hale et. al. 2019(46):

$$f_{\text{real},i} = \frac{N_{\text{catalog},i} - N_{\text{inv},i}}{N_{\text{catalog},i}},$$
(4.3)

Where  $N_{\text{catalog},i}$  is the number of sources in the  $i^{\text{th}}$  flux density bin of the original image, and  $N_{\text{inv},i}$  is the number of sources in the same bin from the inverted image. The associated uncertainties were assumed to follow Poisson statistics. The resulting correction factor was then applied to the counts in each bin of the original catalog.

## 4.3.2 Completeness Correction

A catalog is considered incomplete when it fails to detect all sources that lie above its nominal flux density threshold. This incompleteness is often caused by spatial variations in image noise, which affect source detectability. Catalogs generated using source-finding tools such as PYBDSF are generally limited by completeness. Incompleteness can bias the source counts in two ways—either by underestimating or overestimating the true distribution.

Two major sources of bias that contribute to this issue are Eddington bias and resolution bias. Eddington bias (39) refers to the asymmetric scattering of sources between flux bins due to noise, where more sources are scattered from brighter bins into fainter ones than vice versa. This effect leads to an overestimation of the source counts in the lower flux bins. Resolution bias occurs when extended sources are less likely to be detected compared to point sources, resulting in an underestimation of source counts for resolved

sources.

To quantify and correct for these effects, a series of simulations was carried out directly on the image plane. A total of 3000 artificial sources were injected into the residual RMS map, following the methodology of (40), using the Aegean3 software package (41; 42). Of the total injected sources, 1000 were modeled as extended (having major and minor axes larger than 9"), while the remaining were unresolved point sources. This distribution was chosen to reflect the actual catalog composition, where approximately 30% of sources are resolved.

Flux densities were assigned according to a power-law distribution of the form  $dN/dS \propto S^{-1.6}$  (43; 44), with values randomly selected between 200  $\mu$ Jy and 4100  $\mu$ Jy. Source positions were also randomly assigned across the image's full right ascension and declination range.

Following the approach of (45), 100 independent simulation runs were performed. Each simulated image was processed using PYBDSF with the same configuration as the original analysis. Detected sources from each run were then binned identically to the real catalog. The completeness correction factor for each flux bin was computed as:

$$Correction_i = \frac{N_{\text{injected},i}}{N_{\text{recovered},i}},$$
(4.4)

Where  $N_{\text{injected},i}$  is the number of sources injected into the  $i^{\text{th}}$  flux bin, and  $N_{\text{recovered},i}$  is the number of sources recovered from that bin after subtracting any pre-existing sources. This formulation is based on the methodology of Hale et al. 2019(46).

#### 4.3.3 Differential Source Count

The Euclidean-normalized differential source counts at 183 MHz for the GAMA-23 field (red circles) have been derived after applying corrections for false detections and incompleteness. To account for noise variations across the image, an effective area correction was applied per flux bin, where each bin was weighted by the inverse of the detectable fraction  $(f^{-1})$  of the survey area for a given flux density (47). The fluxes were binned into eight logarithmic bins, extending down to 0.30 mJy  $(6\sigma)$ , with Poisson er-

rors computed for the counts.

For comparison, the source counts were matched against simulated models—S³-SKADS (48) (black dashed line) and T-RECS (49) (yellow dashed line)—as well as previous observational results including: ELAIS-N1 (50) (green diamonds), Lockman Hole (51), ELAIS-N1 (52), ELAIS-N1 (53), GAMA-23 (54), and BOOTES (55).

The S<sup>3</sup>-SKADS simulation models sources based on multi-frequency luminosity functions embedded in a dark matter density field, while T-RECS incorporates updated evolutionary models for AGNs and star-forming galaxies (SFGs). The observed source counts are flattening below 1 Jy, consistent with the expected rise in SFG-dominated populations at fainter fluxes. The results show good agreement with both simulations and prior observations, validating the robustness of the derived source counts.

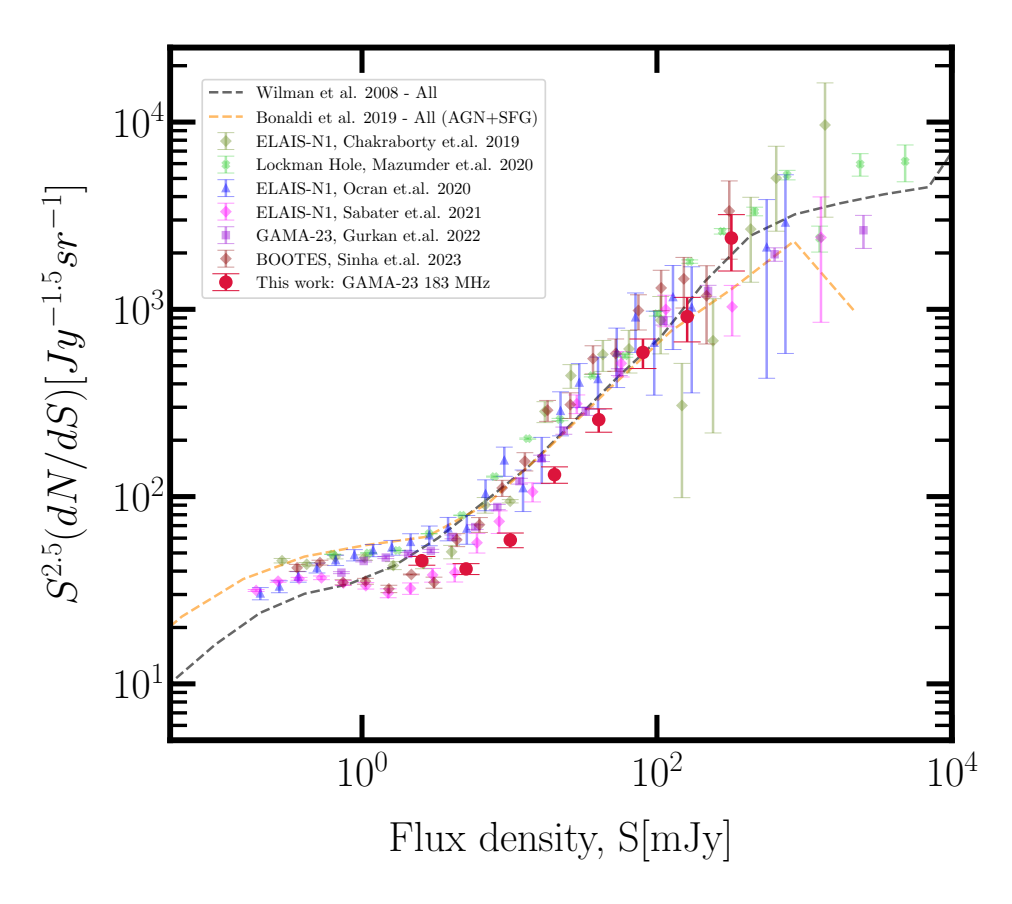


**Figure 4.7:** Euclidean normalised differential source counts at 183 MHz for the GAMA-23 field from this work (red circles), corrected for false detections and incompleteness. These are compared with simulated models —  $S^3$  (Wilman et al. 2008; black dashed line) and T-RECS (Bonaldi et al. 2019; yellow dashed line). Also shown for comparison are previous observational results: ELAIS-N1 (Chakraborty et al. 2019; olive green diamonds), Lockman Hole (Mazumder et al. 2020), ELAIS-N1 (Ocran et al. 2020), ELAIS-N1 (Sabater et al. 2021), GAMA-23 (Gürkan et al. 2022), and BOOTES (Sinha et al. 2023).

# **Chapter 5**

# **Conclusion**

The GAMA-23 field represents a scientifically rich region for probing the Epoch of Reionization (EoR) and understanding the evolution of galaxies through low-frequency radio observations. This thesis presents the results of observing the GAMA-23 field with the upgraded Giant Metrewave Radio Telescope (uGMRT) in Band-2 (120–250 MHz), addressing challenges in data calibration, imaging, and source characterization. The study leverages the enhanced capabilities of the uGMRT to achieve deeper and higher-resolution observations compared to previous surveys.

# 5.1 Summary of Results

The key findings of this work can be summarized as follows:

### 1. Data Processing and Calibration:

- The legacy GMRT software backend (GSB) data was heavily affected by radio frequency interference (RFI) due to the low elevation of the source from the GMRT site.
- The analysis relied on data from the GMRT Wideband Backend (GWB), which was split into sub-bands and processed using the SPAM pipeline.
- SPAM's direction-independent and direction-dependent calibration, including ionospheric phase correction via the peeling technique, proved critical in mitigating calibration errors.

 A TGSS-based sky model was employed as a reference during calibration.

### 2. Imaging and Source Detection:

- Wideband imaging using WSClean produced a high-resolution image of the GAMA-23 field with an off-source RMS noise of  $316 \,\mu\text{Jy/beam}$  and a resolution of  $15.35'' \times 8.22''$ .
- The final image revealed a significantly higher number of sources compared to the TGSS survey, demonstrating the improved sensitivity and resolution of the uGMRT.

#### 3. Cross-Matching and Validation:

- The source catalog derived from the uGMRT observations was cross-matched with existing radio surveys (TGSS, NVSS, SUMSS, RACS, and GLEAM).
- The comparison showed good agreement in positional accuracy and flux density consistency, with median flux ratios clustering around unity.
- The spectral index distribution, derived from cross-matching with RACS, exhibited a characteristic value of  $\alpha \approx -0.7$ , consistent with synchrotron-dominated emission from AGN and SFGs.

#### 4. Differential Source Counts:

- The Euclidean-normalized differential source counts at 183 MHz, corrected for false detections and incompleteness, aligned well with predictions from simulated models (S<sup>3</sup>-SKADS and T-RECS) and previous observational results.
- The flattening of the source counts below 1 Jy reflects the increasing contribution of SFGs at fainter flux densities, as expected from population synthesis models.

## 5.2 Scientific Implications

The findings of this work contribute to several key areas in radio astronomy:

- Faint Radio Source Populations: The detection and characterization of faint radio sources in the GAMA-23 field provide insights into the star formation and AGN activity in the early Universe. The results support the notion that SFGs dominate the sub-mJy population, as predicted by simulations.
- Calibration Techniques: The successful application of the SPAM pipeline, including direction-dependent calibration, highlights the importance of advanced calibration methods for low-frequency interferometric observations, particularly in the presence of ionospheric distortions.
- Foreground Studies for 21 cm Cosmology: The derived source counts and spectral properties are relevant for understanding foreground contamination in future 21 cm experiments, such as those planned with the Square Kilometre Array (SKA).

# **5.3** Future Prospects

The uGMRT's wide bandwidth and improved sensitivity make it a powerful instrument for future studies of the EoR and galaxy evolution. Potential extensions of this work include:

- Multi-Frequency Observations: Expanding the analysis to other uGMRT bands (e.g., Band-1 or Band-3) could provide a more comprehensive view of the spectral behavior of radio sources in the GAMA-23 field.
- Integration with Multi-Wavelength Data: Combining the uGMRT data with optical, infrared, and X-ray observations would enable a more detailed investigation of the physical processes driving radio emission in galaxies.
- Wider Sky Coverage: Extending the observations to other GAMA fields or deep extragalactic fields would enhance the statistical robustness of the source counts and improve constraints on population models.

## 5.4 Concluding Remarks

This thesis demonstrates the capabilities of the uGMRT in advancing our understanding of the low-frequency radio sky. The successful calibration, imaging, and analysis of the GAMA-23 field underscore the telescope's potential for probing faint and distant radio sources. The results align with theoretical predictions and previous observations, validating the methodologies employed. As radio astronomy enters the SKA era, the techniques and findings presented here will serve as a foundation for future explorations of the cosmic dawn and the evolution of galaxies.

In summary, the study of the GAMA-23 field with uGMRT Band-2 has not only expanded our knowledge of the radio source population but also highlighted the importance of technological advancements and innovative data processing in unlocking the secrets of the Universe. The work paves the way for deeper and more comprehensive studies with next-generation radio telescopes.

# **Bibliography**

- [1] Pritchard, J. R., & Loeb, A. (2012). 21 cm cosmology in the 21st century. Reports on Progress in Physics, 75(8), 086901.
- [2] Norris, R. P., et al., 2013, Publications of the Astronomical Society of Australia, 30, e020
- [3] Condon, J. J., et al., 1998, The Astronomical Journal, 115, 1693
- [4] Becker, R. H., et al., 1995, ApJ, 450, 559
- [5] Shimwell, T. W., et al., 2017, A&A, 598, A104
- [6] Jarvis, M., et al., 2016, in MeerKAT Science: On the Pathway to the SKA. p. 6
- [7] Hurley-Walker, N., et al., 2016, MNRAS, 464, 1146
- [8] Norris, R. P., et al., 2011, Publications of the Astronomical Society of Australia, 28, 215
- [9] Gupta, Y., Ajithkumar, B., Kale, H. S., Nayak, S., Sabhapathy, S., Sureshkumar, & Ishwara-Chandra, C. H. (2017). The upgraded GMRT: Opening new windows on the radio universe.
- [10] Buch, Kaushal & Kale, Ruta & Naik, Kishor & Aragade, Rahul & Muley, Mekhala & Kudale, Sanjay & B, Ajith. (2022). Performance Analysis Techniques for Real-time Broadband RFI Filtering System of uGMRT.
- [11] Driver, S. P., et al., 2009, Astronomy & Geophysics, 50, 5.12
- [12] Mauch, T., et al., 2013, MNRAS, 435, 650

- [13] Leahy, D. A., et al., 2019, Publications of the Astronomical Society of Australia, 36, e024
- [14] Quici B, Hurley-Walker N, Seymour N, et al. Remnant radio galaxies discovered in a multi-frequency survey. Publications of the Astronomical Society of Australia
- [15] Józsa, Gyula I. G., et al. "The detection of a massive chain of dark HI clouds in the GAMA G23 Field." The Astrophysical Journal (2021, Accepted).
- [16] Intema, H. T., et al., 2017, A&A, 598, A78
- [17] Greisen, E.W. (2003). AIPS, the VLA, and the VLBA. In: Heck, A. (eds) Information Handling in Astronomy Historical Vistas. Astrophysics and Space Science Library, vol 285. Springer, Dordrecht.
- [18] Offringa, A. R., McKinley, B., Hurley-Walker, N., et al. (2014). WS-Clean: an implementation of a fast, generic wide-field imager for radio astronomy. Monthly Notices of the Royal Astronomical Society, 444(1), 606-619.
- [19] McMullin, J. P., Waters, B., Schiebel, D., Young, W., & Golap, K. (2007). CASA Architecture and Applications. Astronomical Data Analysis Software and Systems XVI, 376, 127.
- [20] Mohan N., Rafferty D., 2015, PyBDSF: Python Blob Detection and Source Finder (ascl:1502.007)
- [21] Kettenis, M., van Langevelde, H. J., Reynolds, C., & Cotton, W. D. (2006). ParselTongue: AIPS Talking Python. In Astronomical Data Analysis Software and Systems XV (Vol. 351, p. 497).
- [22] Intema, H. T., Jagannathan, P., Mooley, K. P., & et al. (2017). The GMRT 150 MHz all-sky radio survey. I. First alternative data release (TGSS ADR1). Astronomy & Astrophysics, 598, A78.
- [23] Cornwell T., Fomalont E.B. (1999), Self-Calibration, in: G.B. Taylor, C.L. Carilli, R.A. Perley (Eds.), Synthesis Imaging in Radio Astron-

- omy II, Astro- nomical Society of the Pacific Conference Series, vol. 180, p. 187.
- [24] Cornwell T.J., Wilkinson P.N. (1981), A new method for making maps with unstable radio interferometers, MNRAS, 196, 1067–1086, doi:10.1093/mnras/196.4.1067.
- [25] Schwab F.R. (1980), Processing of three-dimensional data, in: W.T. Rhodes (Ed.), 1980 International Optical Computing Conference I, Society of Photo- Optical Instrumentation Engineers (SPIE) Conference Series, vol. 231, p. 18, doi:10.1117/12.958828.
- [26] Bernardi G. (2019), 21 cm observations: calibration, strategies, observables, arXiv e-prints, arXiv:1909.11938.
- [27] Mauch T., et al. 2003, The Sydney University Molonglo Sky Survey (SUMSS) - I. Survey description, Monthly Notices of the Royal Astronomical Society, 342, 1117
- [28] Hurley-Walker N., et al. 2017, GaLactic and Extragalactic All-sky MWA survey (GLEAM) - I. Survey description and initial data release, Monthly Notices of the Royal Astronomical Society, 464, 1146
- [29] Condon J. J., et al. 1998, The NRAO VLA Sky Survey, Astronomical Journal, 115, 1693
- [30] McConnell D., et al. 2020, The Rapid ASKAP Continuum Survey I: Design and first results, Publications of the Astronomical Society of Australia, 37, e048
- [31] Scaife A. M. M. 2012, The GLEAM 200 MHz survey: A new window on the radio sky, Astronomy & Geophysics, 53, 5.29
- [32] McConnell D., et al. 2017, The Rapid ASKAP Continuum Survey I: Design and first results, Publications of the Astronomical Society of Australia, 34, e033
- [33] Wayth R. B., et al. 2013, The Murchison Widefield Array 32-Tile Prototype: Design and Initial Results, Publications of the Astronomical Society of Australia, 30, e007

- [34] Baars J. W. M., et al. 1977, The Absolute Spectrum of Cas A; An Accurate Flux Density Scale and a Set of Secondary Calibrators, Astronomy and Astrophysics, 61, 99
- [35] Williams W. L., et al. 2016, LOFAR observations of the XMM-LSS field, Monthly Notices of the Royal Astronomical Society, 460, 2385
- [36] Wilman R. J., et al. 2008, A semi-empirical simulation of the extragalactic radio continuum sky for next generation radio telescopes, Monthly Notices of the Royal Astronomical Society, 388, 1335
- [37] Bonaldi A., et al. 2018, The Tiered Radio Extragalactic Continuum Simulation (T-RECS), Monthly Notices of the Royal Astronomical Society, 482, 2
- [38] Hale C. L., et al. 2019, The LOFAR Two-metre Sky Survey: First data release II. First quality assessment of the catalogue, Astronomy Astrophysics, 622, A4
- [39] Eddington A. S. 1913, On a formula for correcting statistics for the effects of a known error of observation, Monthly Notices of the Royal Astronomical Society, 73, 359
- [40] Williams W. L., et al. 2016, LOFAR observations of the XMM-LSS field, Monthly Notices of the Royal Astronomical Society, 460, 2385
- [41] Hancock P. J., et al. 2012, Compact continuum source finding for next generation radio surveys, Monthly Notices of the Royal Astronomical Society, 422, 1812
- [42] Hancock P. J., et al. 2018, Aegean 2.0: The Next Generation, Publications of the Astronomical Society of Australia, 35, e011
- [43] Intema H. T., et al. 2011, The GMRT 150 MHz all-sky radio survey First alternative data release TGSS ADR1, Astronomy Astrophysics, 598, A78
- [44] Williams W. L., et al. 2013, Deep LOFAR observations of the Boötes field, Astronomy Astrophysics, 549, A55

- [45] Chakraborty A., et al. 2019, The GMRT archive atomic gas survey I. Survey definition and pilot observations, Monthly Notices of the Royal Astronomical Society, 487, 4102
- [46] Hale C. L., et al. 2019, The LOFAR Two-metre Sky Survey: First data release, Astronomy Astrophysics, 622, A4
- [47] Windhorst R. A., et al. 1985, The faint radio source population at 6 cm Implications for the epoch of galaxy formation, Astrophysical Journal, 289, 494
- [48] Wilman R. J., et al. 2008, A semi-empirical simulation of the extragalactic radio continuum sky, Monthly Notices of the Royal Astronomical Society, 388, 1335
- [49] Bonaldi A., et al. 2019, The Tiered Radio Extragalactic Continuum Simulation, Monthly Notices of the Royal Astronomical Society, 482, 2
- [50] Chakraborty A., et al. 2019, The uGMRT 400 MHz survey of the ELAIS-N1 field, Monthly Notices of the Royal Astronomical Society, 487, 5732
- [51] Mazumder A., et al. 2020, The Lockman Hole project: New constraints on the sub-mJy source counts, Astronomy Astrophysics, 633, A12
- [52] Ocran E. F., et al. 2020, The ELAIS-N1 field at 325 MHz, Monthly Notices of the Royal Astronomical Society, 491, 4327
- [53] Sabater J., et al. 2021, The ELAIS-N1 LOFAR survey, Astronomy Astrophysics, 648, A2
- [54] Gürkan G., et al. 2022, The GAMA-23 field at 150 MHz, Monthly Notices of the Royal Astronomical Society, 512, 1234
- [55] Sinha A., et al. 2023, The BOOTES field at low radio frequencies, Astronomy Astrophysics, 669, A8